Riv. Mat. Univ. Parma, Vol. **4** (2013), 345-396

AURELIO PATELLI and STEFANO RUFFO

Statistical mechanics and dynamics of long-range interacting systems

Abstract. This manuscript summarizes the content of a series of five lectures given by one of the authors (SR) at the summer school on *Methods and Models of Kinetic Theory* in Porto Ercole, june 3-9 2012. The paper is organized in four Sections. In the first, introductory, Section 1 we discuss several physical systems in which long-range interactions appear: self-gravitating systems, mean-field spin systems, Euler's equation in two dimensions, one component electron plasmas, dipolar systems, finite systems, free electron lasers, cold atoms in optical cavities. The following Section 2 is devoted to ensemble inequivalence, which manifests itself with exotic phenomena like negative specific heat, temperature jumps, broken ergodicity. In this Section we present illustrative models for which microcanonical entropy can be obtained by direct counting: the Blume-Capel and the Kardar-Nagel model. In Section 3 we describe how large deviation theory can be used to obtain the microcanonical entropy of several mean-field models, especially those with continuous local variables, for which direct counting is not applicable. Here, we also show how magnetic susceptibility can become negative in the microcanonical ensemble. Finally, Section 4 is fully devoted to describe quasistationary states. These are non equilibrium states that appear generically in the dynamics of system with long-range interactions and for which a beautiful statistical theory has been proposed long ago by Lynden-Bell. The results presented in this set of lectures are mainly contained in Refs. [**1, 2, 3**].

Keywords. Long-range interactions, Inequivalence of ensembles, Large deviations, Quasistationary states.

Mathematics Subject Classification (2010): 82B05, 82B26, 82C05, 82C22.

Received: February 4, 2013; accepted: April 10, 2013.

This research was partially supported by INFN under contract MI41 and by ANR-France under Chaire d'Excellence project ANR-10-CEXC-010-01.

Contents

1 - Introduction

Various definitions of long-range interactions have been adopted in the literature. Here, we will choose the one that is related to the extensive properties of the energy. An interaction is defined to be long-range if the two-body potential at large interparticle distance behaves as

$$V(r) \sim J r^{-\alpha}$$
$$0 \leq \alpha \leq d\,,$$

with d the dimension of the embedding space and J the strength of the coupling. For such interactions the energy per particle ε scales as

$$\varepsilon = \frac{E}{N} = \int_{\delta}^{R} d^d r \rho \frac{J}{r^\alpha} = \frac{\rho J \Omega_d}{d-\alpha}\left[R^{d-\alpha} - \delta^{d-\alpha}\right], \tag{1}$$

where δ is a small distances cut-off, R is the cut-off at large distances, ρ is a mass (or charge) density and Ω_d is the angular volume in dimension d. It is then straightforward to check that

- if $\alpha > d$ then $\varepsilon \to const$ when $R \to \infty$
- if $0 \leq \alpha \leq d$ then $\varepsilon \sim V^{1-\alpha/d}$ ($V \sim R^d$).

In terms of the extensive energy $E = \varepsilon V$, where V is volume,

$$\alpha > d \quad E \sim V$$
$$\alpha \leq d \quad E \sim V^{2-\alpha/d},$$

and the free energy

$$F = E - TS \quad , \quad S \sim V, \tag{2}$$

with T the intensive temperature and S the entropy, that typically scales with the volume. Therefore, thermodynamic properties of long-range systems are dominated by the energy E, which scales with volume V faster than linear. A way out from this energy dominance was proposed by Marc Kac. It consists in scaling the coupling

constant

$$J \to JV^{\alpha/d-1}\,. \tag{3}$$

In this way the free energy turns out to be extensive in the volume

$$F \sim V\,. \tag{4}$$

However, this is a "mathematical trick" and doesn't correspond to any physical effect: no interaction that changes its strength when varying the volume is known. This trick can be adopted only for the sake of performing a meaningful large volume limit. Once the free energy per particle is obtained, the physical description can be retrieved by scaling back the coupling constant.

Alternatively, one can rescale the temperature

$$T \to TV^{1-\alpha/d} \tag{5}$$

and then the free energy scales superlinearly in the volume

$$F \sim V^{2-\alpha/d}\,. \tag{6}$$

Let us illustrate these features quantitatively for a case of interest in astrophysics: globular clusters, see Fig. 1. These are gravitationally bound concentrations of approximately $10^4 - 10^6$ stars, spread over a volume from several tens to about 200 light years in diameter (1 light year $= 9.4 \cdot 10^{15} m$). For a typical globular cluster (M2): $N = 1.5 \cdot 10^5$, $R = 175$ light years, $M = 2 \cdot 10^{30}$ Kg.

Fig. 1. The spherically symmetric mass distribution of stars in a globular cluster.

An order of magnitude estimate of energy and entropy gives

$$E = \frac{GN^2M^2}{R} \quad , \quad S = k_B N \quad , \quad \frac{E}{S} \sim \frac{GNM^2}{k_B R} \sim 1.7 \cdot 10^{60} K \tag{7}$$

where G is Newton's gravitational constant and k_B is Boltzmann's constant. To this extremely high temperature, one can associate a velocity by energy equipartition (neglecting here interactions)

$$v = \sqrt{\frac{3k_B T}{M}} \approx 5.9\, Km/s\,. \tag{8}$$

Typical star velocities are indeed in a range between few Km/s up to $100 Km/s$. This example shows that energy can compete with entropy, although $E \sim V^{5/3}$, provided temperature is big enough.

Although one can get an extensive energy using Kac's trick, this is not necessarily additive. This concept can be easily illustrated by considering the Curie-Weiss model of magnetism

$$H^N_{CW} = -\frac{J}{2N}\sum_{i,j}\sigma_i\sigma_j\,, \tag{9}$$

where $\sigma_i = \pm 1$ is a spin variable. It is a mean-field model, which can be considered as the $\alpha = 0$ limit of long-range interacting systems. The coupling is rescaled using Kac's trick.

Let us consider a macrostate having zero magnetization $M = \sum_i \sigma_i = 0$, composed of $N/2$ spin 1 sites and $N/2$ spin -1 sites, Fig. 2. Since the energy is proportional to the square of magnetization, the total energy of the system is $E_{I+II} = 0$. However, the energy of the two parts $E_I = E_{II} = -J/8N$ does not vanish and, therefore, $E_{I+II} \neq E_I + E_{II}$.

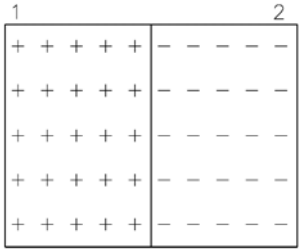

Fig. 2. A zero magnetization macrostate divided into two subsystems of positive and negative magnetization, respectively.

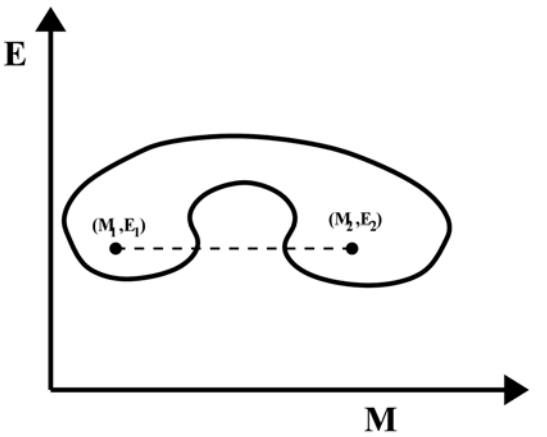

Fig. 3. Non convex shape of the region of accessible macrostates in the magnetization/ energy plane for long-range systems.

The violation of additivity is crucial in determining the thermodynamic properties of systems with long-range interactions. For instance, it determines a violation of convexity of the domain of accessible macrostates. An example is shown in Fig. 3, where the boundary of the region of accessible macrostates is represented by the thick line with the shape of a bean. In standard thermodynamics, for short range interactions, all states satisfying

$$E = \lambda E_1 + (1-\lambda)E_2 \quad , \quad M = \lambda M_1 + (1-\lambda)M_2 \quad , \quad 0 \leq \lambda \leq 1 \tag{10}$$

must be present at the macroscopic level, because additivity is satisfied. This is in general not true for long-range interactions. This can determine a violation of ergodicity in the microcanonical ensemble as we will discuss in Section 2.

The use of the canonical ensemble in system with long-range interactions is doubtful, because its classical derivation from the microcanonical ensemble is based on additivity. Let us briefly recall it. The microcanonical partition function for a system composed by N particles in dimension $d = 3$ is defined as

$$\Omega(E) = \int \frac{d^{3N}q\, d^{3N}p}{h^{3N}} \delta(E - H(p,q)) \,, \tag{11}$$

where (q,p) are canonically conjugate variable, H is the Hamiltonian and h is Planck's constant. Entropy is defined as

$$S(E) = k_B \ln \Omega(E) \,, \tag{12}$$

where an ineffective energy scale should be included in the logarithm. Using additivity, the probability density that a subsystem composed of N_1 particles has

energy E_1 is

$$p(E_1) = \frac{\Omega_1(E_1)\Omega_2(E-E_1)}{\int dE_1 \Omega_1(E_1)\Omega_2(E-E_1)} \,. \tag{13}$$

If the subsystem is much smaller than the system $E \gg E_1$, $N \gg N_1$

$$S_2(E-E_1) = S_2(E) - E_1 \frac{\partial S_2}{\partial E_2}\bigg|_E + \frac{1}{2}E_1^2 \frac{\partial^2 S_2}{\partial E_2^2}\bigg|_E + \cdots \,, \tag{14}$$

where $E_2 = E - E_1$. Using this Taylor expansion, one can prove that

$$p(E_1) = \frac{\Omega_1(E_1)\exp(-\beta E_1)}{\int dE_1 \Omega_1(E_1)\exp(-\beta E_1)} = \frac{\Omega_1(E_1)\exp(-\beta E_1)}{Z} \,, \tag{15}$$

if $N_2 = N - N_1 \gg N_1$, where

$$\beta = \frac{1}{k_B T} = \frac{\partial S_2}{\partial E_2}\bigg|_E \tag{16}$$

is the inverse temperature.

In the following, we will consider both the microcanonical (11) and the canonical distribution (15). In order to justify the use of the canonical distribution for systems with long-range interactions, that are non additive, one must resort to an alternative physical interpretation. For instance, consider that the system is in interaction with an external bath of a different nature, e.g. stochastic.

Models with long-range interactions can represent systems of interacting particles having the following potential energy

$$U(\vec{r}_1, \ldots, \vec{r}_N) = \sum_{1 \le i < j \le N} V(|\vec{r}_i - \vec{r}_j|) + g \sum_{i=1,N} V_e(\vec{r}_i) \,, \tag{17}$$

where $\vec{r}_i$ is the position of the ith particle, V the interparticle potential and V_e an external field.

Alternatively, long-range interactions can be defined on a lattice

$$U(\mathbf{q}_1, \ldots, \mathbf{q}_N) = \sum_{1 \le i < j \le N} C_{ij} V(\mathbf{q}_i, \mathbf{q}_j) + g \sum_{i=1}^{N} V_e(\mathbf{q}_i) \tag{18}$$

where $\mathbf{q}_i$ represents the "internal" degrees of freedom sitting at a lattice site $\mathbf{r}_i$ and the coupling

$$C_{ij} = \frac{1}{|\vec{r}_i - \vec{r}_j|^\alpha} \qquad , \quad 0 \le \alpha \le d \tag{19}$$

bears the long-range nature of the interaction.

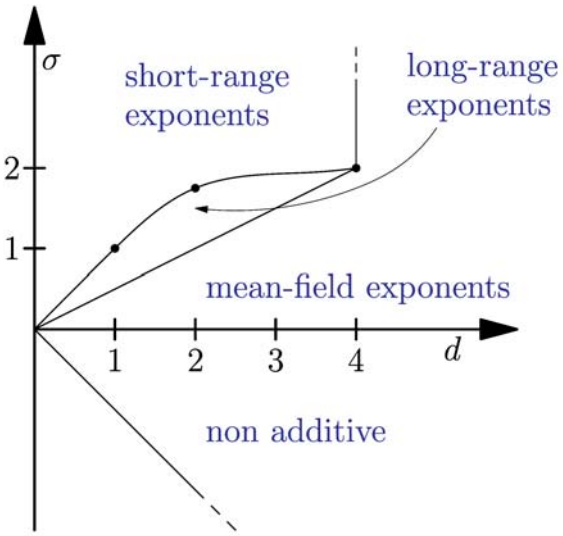

Fig. 4. Different behaviors of long-range systems depending on dimension d and the exponent $\sigma = \alpha - d$.

Defining $\alpha = d + \sigma$ one can identify different regions in the d, σ plane (see Fig. 4). The non additive long-range region has $-d \leq \sigma \leq 0$, as discussed above. However, the long-range behavior extends to $\sigma > 0$, although the energy is here additive. It can be shown that, if $0 < \sigma \leq d/2$ the critical behavior is characterized by mean-field (classical) exponents, exactly as for the full region $d > 4$ (any value of σ). Moreover, in a region $\sigma > d/2$ and below a given line which is only partially known, the system maintains some long-range features, but with non classical σ-dependent critical exponents. Some points along this line are known. At $d = 1$ the line passed through $\sigma = 1$: indeed in the whole range $0 \leq \sigma \leq 1$ one can have phase transitions in one dimension. For $d = 2$, numerical simulations show that the line passes through $\sigma = 7/4$. Finally, renormalization group techniques suggest that the line reaches $\sigma = 2$ from below at $d = 4$. Above this line and below $d = 4$ the system becomes short-range.

A model with Hamiltonian of the type of (18) has been introduced by Dyson. An Ising spin variable $\sigma_i = \pm 1$ sits on the ith site of a one-dimensional lattice with N sites and the Hamiltonian is

$$H^N_{Dyson} = -\frac{J}{2} \sum_{i \neq j = 1}^{N} \frac{\sigma_i \sigma_j}{|i - j|^{1+\sigma}} \,. \tag{20}$$

The scaling properties of the energy are

$$\begin{aligned} &\sigma > 0 \quad E \sim N\,, \\ &-1 \leq \sigma \leq 0 \quad E \sim N^{1-\sigma}\,. \end{aligned}$$

The model is known to display a ferromagnetic phase transition for $0 < \sigma \leq 1$ and no phase transition for $\sigma > 1$. This is in accordance with a theorem due to Dyson and Ruelle. At $\sigma = 1$ it has been proved that a jump in magnetization at the transition point is present, together with a diverging length and correlations decay as a power law of the distance.

For $-1 \leq \sigma \leq 0$, one can apply Kac's rescaling

$$J \to \widetilde{J} = JN^{\sigma} \tag{21}$$

and get an extensive free energy $F = E - TS \sim N$. In this range of values of σ one can prove that a continuum limit exists, meaning that for Hamiltonian (20) the following property holds

$$\widetilde{H}_{Dyson} = NH_{Dyson}[m] + o(N) \tag{22}$$

where

$$H_{Dyson}[m] = -\frac{J}{2}\int_0^1 dr \int_0^1 dr' \, \frac{m(r)m(r')}{|r - r'|^{1+\sigma}} \tag{23}$$

is a functional of the local magnetization m, with $r \in [0,1]$. The proof of this results relies on dividing the lattice in K boxes, each of side length $l = N/K$ and introduce a box-averaged magnetization m_k, $k = 1, \ldots K$. In the limit $N \to \infty$, $K \to \infty$, $K/N \to 0$ the magnetization becomes a continuous function of r. The construction can be easily generalized to higher dimensional lattices and to other types of interactions.

The most notable and fundamental example of long-range interaction is gravity, for which the potential energy is

$$U(\vec{r}_1, \ldots, \vec{r}_N) = -Gm^2 \sum_{1 \leq i < j \leq N} \frac{1}{|\vec{r}_i - \vec{r}_j|}\,. \tag{24}$$

In order to get a finite microcanonical partition sum, one has to confine the self-gravitating system in a box of volume V. This is necessary also when doing the statistical mechanics of the perfect gas. Hence,

$$\Omega(E) = \int_V \prod_i d\vec{r}_i d\vec{p}_i \delta(E - K - U) \propto \int_V \prod_i d\vec{r}_i (E - U)^{(3N-2)/2}\,, \tag{25}$$

where K is kinetic energy and a first integration over momenta has been performed. The integral in (25) behaves as $r_{ij}^{4-3N/2}$ when $r_{ij} = |\vec{r}_i - \vec{r}_j| \to 0$, i.e. when two bodies get close. Hence, it diverges for $N \geq 3$, determining a divergence of microcanonical entropy $S(E) = k_B \ln \Omega(E)$ (similarly, the canonical partition function diverges). There is no way to prevent this short-distance divergence other than regularizing Newtonian potential. This can be done in different ways: softening, hard-core, Pauli exclusion. Irrespective of the way gravitational potential is regularized, the non-additive features related to the long-range nature of the interaction persist. These are significantly represented by the presence of negative specific heat. This phenomenon can be heuristically justified using virial theorem, which for the gravitational potential reads

$$\langle K \rangle = -\frac{1}{2}\langle U \rangle \quad , \quad \langle K \rangle = -E \tag{26}$$

where $\langle \cdot \rangle$ denotes a temporal average. Since kinetic energy K is always positive, it is clear that this theorem can only be valid for bound states, for which E is negative. Using equipartition theorem, average kinetic energy is proportional to temperature and, hence, the second identity in (26) tells us that specific heat c_V, which is proportional to dE/dT, is indeed negative. However, this is just handwaving and this type of argument uses plenty of hypotheses. More rigorously, it can be shown that regularized self-gravitating systems confined in a box have an entropy that is a non concave function of the energy, as shown in Fig. 5a. Since specific heat is related to the second derivative of the entropy with respect to energy

$$\partial^2 s/\partial \varepsilon^2 = -(c_V T^2)^{-1} \, , \tag{27}$$

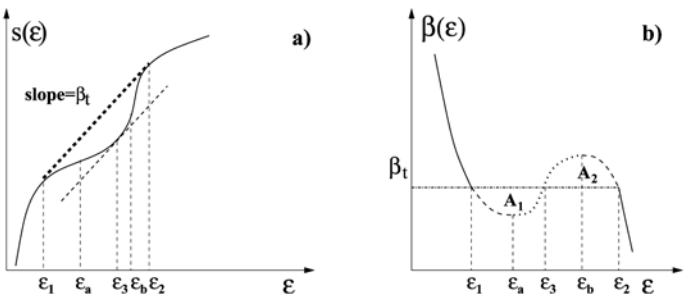

Fig. 5. a) Schematic shape of microcanonical entropy per particle $s = S/N$ as a function of energy per particle $\varepsilon = E/N$ (solid line) showing a "globally" convex region in the range $[\varepsilon_1, \varepsilon_2]$, the thick dashed line realizes the "concave envelope". b) Inverse temperature β as a function of ε. According to the Maxwell's constructions the areas $A_1 = A_2$. The curve $\beta(\varepsilon)$ represents states that are stable (solid line), unstable (dotted line) and metastable (dashed lines).

it follows that in the energy range $[\varepsilon_a, \varepsilon_b]$, where the entropy is convex, specific heat must be negative. For short-range additive interactions all states within the wider range $[\varepsilon_1, \varepsilon_2]$ would have an entropy that is represented by thick dashed line in Fig. 5a. In Fig. 5b, the inverse temperature β is plotted as a function of ε, in the negative specific heat region, temperature decreases as energy increases.

Another important example of a system with long-range interactions is Euler's equation in two dimensions

$$\frac{\partial \vec{v}}{\partial t} + (\vec{v} \cdot \overrightarrow{\nabla})\vec{v} = 0 \quad , \quad \overrightarrow{\nabla} \cdot \vec{v} = 0 \quad , \quad \vec{v} = (v_x, v_y)\,. \tag{28}$$

Using vorticity

$$\omega(x,y) = \frac{\partial v_y}{\partial x} - \frac{\partial v_x}{\partial y}\,, \tag{29}$$

Euler's equation can be rewritten as

$$\frac{\partial \omega}{\partial t} + \vec{v} \cdot \overrightarrow{\nabla}\omega = 0\,. \tag{30}$$

The long-range features of this equation are made explicit introducing the stream function $\psi(x,y)$

$$v_x = +\frac{\partial \psi}{\partial y}$$
$$v_y = -\frac{\partial \psi}{\partial x}\,.$$

This function is directly related to vorticity by the Poisson equation

$$\omega = -\Delta\psi\,. \tag{31}$$

whose solution in a given domain D is

$$\psi(\vec{r}) = \int_D d\vec{r}'\ \omega(\vec{r}')\ G(\vec{r},\vec{r}')\,. \tag{32}$$

In the infinite domain, the Green function is

$$G(\vec{r},\vec{r}') = -\frac{1}{2\pi}\ln|\vec{r}-\vec{r}'|\,, \tag{33}$$

which decays in space slower than any power of the distance, the α exponent would be here equal to zero. One can also easily show the non additive features of the energy

$$E = \int_D d\vec{r}\frac{1}{2}(v_x^2 + v_y^2) \quad = \quad \int_D d\vec{r}\frac{1}{2}(\nabla\psi)^2 \quad = \quad \frac{1}{2}\int_D d\vec{r}\ \omega(\vec{r})\psi(\vec{r})$$
$$= -\frac{1}{4\pi}\int_D\int_D d\vec{r}d\vec{r}'\ \omega(\vec{r}')\omega(\vec{r})\ln|\vec{r}-\vec{r}'|$$

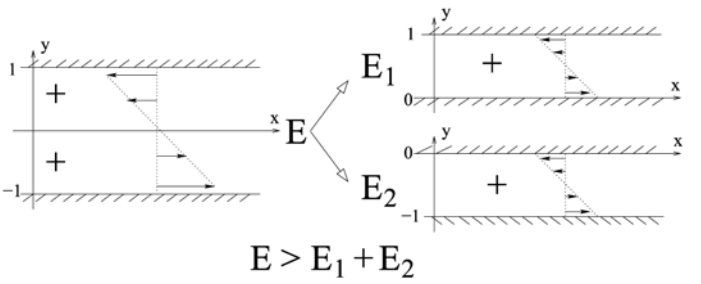

Fig. 6. An example showing the non additivity of energy in the Euler equation for a shear flow.

for the shear flow

$$v_x = -y \quad , \quad v_y = 0 \quad , \quad \omega = 1 \quad , \quad \psi = -y^2/2 \, . \tag{34}$$

The energy per length L, E/L, along x of the flow within $-1 \leq y \leq 1$ is larger than the energy of the separate flows: $-1 \leq y \leq 0$, $0 \leq y \leq 1$

$$\frac{E}{L} = \frac{1}{3} \quad , \quad \frac{E_{1,2}}{L} = \frac{1}{24} \, . \tag{35}$$

Coulomb systems are another example of long-range interactions

$$U(\vec{r}_1, \ldots, \vec{r}_N) = \frac{1}{4\pi\varepsilon_0} \sum_{i<j}^{N} e_i e_j V(|\vec{r}_i - \vec{r}_j|) \, , \tag{36}$$

where ε_0 is the vacuum permittivity and e_i is the charge located at $\vec{r_i}$. For such systems, it can be shown that the excess charge is expelled to the boundary of the domain and the bulk is neutral. A typical configuration has a distribution of charges of equal sign surrounded by a "cloud" of particles of opposite charge, which "screen" the interaction at long-range. The effective two-body potential is therefore

$$V_{eff} \propto \frac{\exp(-r/\lambda_D)}{r} \, , \tag{37}$$

where $\lambda_D = (\varepsilon_0/(2ne^2\beta))^{1/2}$ is the Debye length and n is particle density. Coulomb systems are effectively short-range. Rigorous proofs of this result exist only at low density and high temperature.

A plasma of electrons can be confined by a crossed electric **E** and magnetic **B** field. As shown in Fig. 7 the electrons are contained axially by negative voltages and radially by a uniform axial magnetic field B_z. At the temperature and density of the experiment, electrons are collisionless. They bounce axially very rapidly and drift

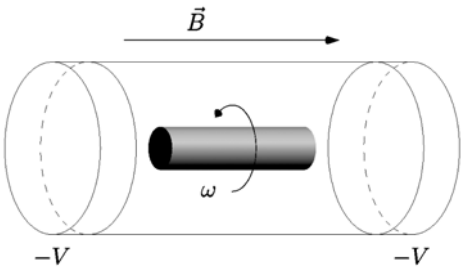

Fig. 7.

across the magnetic field with velocity

$$\mathbf{v} = \frac{-\nabla\phi \times \hat{z}}{B_z} \,. \tag{38}$$

As for an effectively incompressible fluid, electron density $n(x, y)$ obeys the evolution equations

$$\frac{\partial n}{\partial t} + \mathbf{v} \cdot \nabla n = 0 \tag{39}$$

$$\Delta\phi = \frac{en}{\varepsilon_0} \,, \tag{40}$$

where $-e$ is electron charge. These equations are isomorphic to the two dimensional Euler equation with vorticity $\omega = en/\varepsilon_0$ and stream function $\psi = \phi/B_z$. In some sense, the electron plasma is the best experimental realization of 2D incompressible inviscid fluids. Dipolar interaction is marginally long-range, $\alpha = 3$ in $d = 3$. The interaction energy of two dipoles is

$$E_{ij} = \frac{\mu_0}{4\pi}\left[\frac{\vec{\mu}_i \cdot \vec{\mu}_j}{|\vec{r}_{ij}|^3} - \frac{3(\vec{\mu}_i \cdot \vec{r}_{ij})(\vec{\mu}_j \cdot \vec{r}_{ij})}{|\vec{r}_{ij}|^5}\right] , \tag{41}$$

where μ_0 is vacuum permeability and $\vec{\mu}_i$ is the dipolar moment at site i. Because of the anisotropy of the interaction, dipolar systems are strongly frustrated: several configurations have the same energy. For ferromagnetic samples of ellipsoidal shape

$$H^N_{Dipolar} = \frac{1}{2}\sum_{i,j} E_{ij} = E_0 V + \frac{1}{2}\mu_0 \frac{\left(\sum\limits_i \vec{\mu}_i\right)^2}{V} D \tag{42}$$

where E_0 is a local energy depending on crystal structure and D is the so-called shape-dependent demagnetizing factor: $D = 1/3$ for spherical samples, $D = 0$ for needle shape samples, $D = 1$ for disk shaped samples. An important result is due to Griffiths: The free energy of a dipolar magnetic system is shape-independent. This

implies that the macroscopic state cannot be ferromagnetic. However, ferromagnetism can exist in mesoscopic samples, paving the way to the possible experimental detection of long-range effects.

Even if the interactions are short-range, systems of linear size comparable with the range of the interaction are non-additive. Examples are: atomic clusters, quantum fluids, large nuclei, dense hadronic matter. Atomic clusters of a few atoms show phase transitions: both solid-liquid and liquid-gas. Their signatures are: the bimodality of the density of states as a function of energy; the negative slope of the microcanonical caloric curve, i.e. negative specific heat; large fluctuations in the partition of potential and kinetic energy; approach to the real axis of the zeroes of the partition sum as a function of complex temperature in the canonical ensemble.

Experiments have been performed which claim to have found signatures of negative specific heat. The first set of experiments is realized using atomic sodium clusters Na^{+}_{147} and hydrogen cluster ions $H^{+}_{3}(H_2)_{m\leq 14}$. In the first case, negative specific heat has been found in correspondence with a solid-liquid phase transition, while in the second case in the vicinity of a liquid-gas transition. Sodium clusters are produced in a gas aggregation source and then thermalized with Helium gas of con-

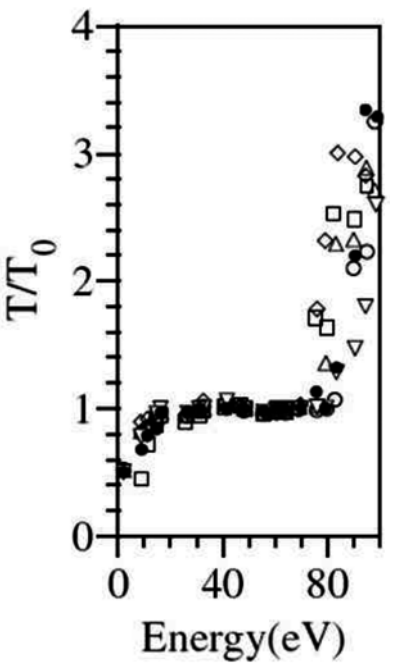

Fig. 8. Temperature vs. energy in a hydrogen cluster experiment, showing a region of negative specific heat.

trolled temperature and selected to a single cluster size by a first mass spectrometer. The energy of the clusters is then increased by laser irradiation leading finally to evaporation. A second mass spectrometer allows the reconstruction of the size distribution, and correspondingly of their energies. Performing this experiment at different temperatures of the Helium gas, a temperature-energy relation, so-called caloric curve, is determined. In the second set of experiments on nuclear fragmentation, the presence of negative specific heat is inferred from the event by event study of energy fluctuations in excited Au nuclei resulting from Au + Au collisions. The data seem to indicate a negative specific heat at an excitation energy around 4.5 MeV/u. In the third set of experiments, performed with hydrogen cluster ions, the energy and the temperature are determined from the size distribution of the fragments after collision of the cluster with a Helium projectile. The experiments, see Fig. 8, show a negative specific heat region, corresponding to a liquid-gas transition.

An experimental apparatus where long-range forces are at play is the free electron laser. In the linear free electron laser, a relativistic electron beam propagates through a spatially periodic magnetic field, interacting with the co-propagating electromagnetic wave, see Fig. 9. Lasing occurs when the electrons bunch in a subluminar beat wave. After scaling away the time dependence of the phenomenon and introducing appropriate variables, e.g. the length z along the lassoing direction, it is possible to catch the essence of the asymptotic state by studying the following equations of motion, first introduced by Colson and Bonifacio,

$$\begin{aligned}
\frac{d\theta_j}{dz} &= p_j \\
\frac{dp_j}{dz} &= -\mathbf{A}e^{i\theta_j} - \mathbf{A}^* e^{-i\theta_j} \\
\frac{d\mathbf{A}}{dz} &= i\delta\mathbf{A} + \frac{1}{N}\sum_j e^{-i\theta_j} ,
\end{aligned}$$

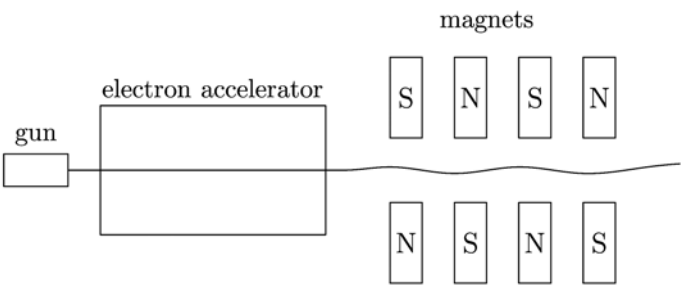

Fig. 9. Sketch of a linear free electron laser.

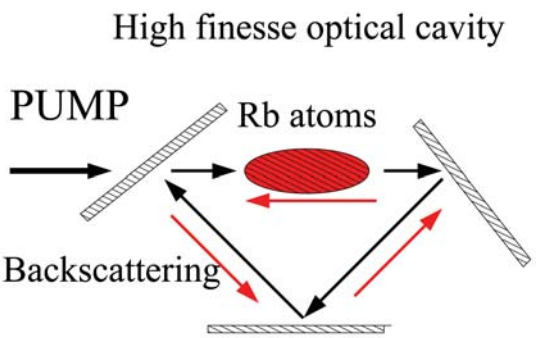

Fig. 10. Collective interactions between light and cold atoms.

which derive from the Hamiltonian

$$H_{FEL}^{N} = \sum_{j=1}^{N} \frac{p_j^2}{2} - N\delta A^2 + 2A \sum_{j=1}^{N} \sin(\theta_j - \varphi)\,. \tag{43}$$

The p_i's are related to the energies relative to the center of mass of the N electrons and the conjugated variables θ_i characterize their positions with respect to the co-propagating wave. The complex electromagnetic field variable, $\mathbf{A} = A\, e^{i\varphi}$, defines the amplitude and the phase of the dominating mode ($\mathbf{A}$ and $\mathbf{A}^\star$ are canonically conjugate variables). The parameter δ measures the average deviation from the resonance condition.

Essentially the same Hamiltonian (43) describes the phenomenon called Collective Atomic Recoil Lasing (CARL). The experimental setup is displayed in Fig. 10. A cold atomic gas is enclosed in a high finesse optical cavity. Above a critical pump beam (black) intensity, a probe backscattered beam (red) switches on a reaches a saturation level. A full modelisation of the phenomenon requires a description of the internal atomic dynamics, the atomic center of mass dynamics and the optical field dynamics. In the simplified model (43) θ_j is the phase of atom j in the optical potential, p_j is the scaled momentum of the atom and A is the probe field amplitude.

2 - Ensemble inequivalence

For systems with long-range interactions statistical ensembles can be inequivalent. For instance, the temperature-energy relation might not be the same in the microcanonical and canonical ensemble. In the microcanonical ensemble specific heat can be negative.

Let us first illustrate the case in which ensembles are indeed equivalent. It means that free energy can be obtained by Legendre-Fenchel transforming entropy and that entropy is itself the Legendre-Fenchel transform of free energy

$$\phi(\beta) = \beta f(\beta) = \inf_{\varepsilon} [\beta\varepsilon - s(\varepsilon)] \quad , \quad s(\varepsilon) = \inf_{\beta} [\beta\varepsilon - \phi(\beta)] \, , \tag{44}$$

where $f(\beta)$ is free energy and $\phi(\beta)$ the rescaled free energy. This involutive property is shown in Fig. 11.

This relation is a consequence of a saddle-point limit $N \to \infty$ in the following formula

$$\begin{aligned} \exp(-\beta N f(\beta)) = & Z(\beta) = \int dE \int \frac{dq^{3N} dp^{3N}}{h^{3N}} \, \delta(H(p,q) - E) \exp(-\beta E) \\ & = \int dE \, \Omega(E) \exp(-\beta E) = N \int d\varepsilon \, \exp(-N[\beta\varepsilon - s(\varepsilon)]) \, , \end{aligned}$$

where Z is the partition function.

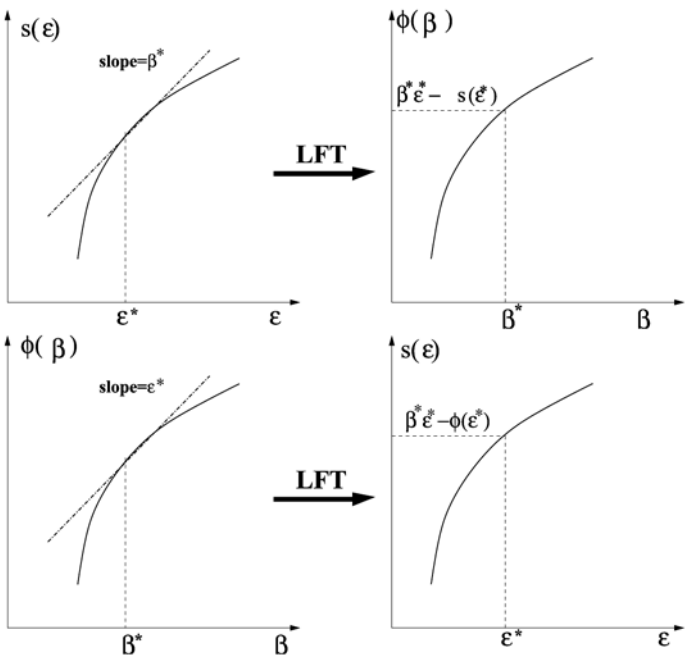

Fig. 11. Upper panel: Free energy from entropy by a Legendre-Fenchel transform. Lower panel: Entropy from free energy.

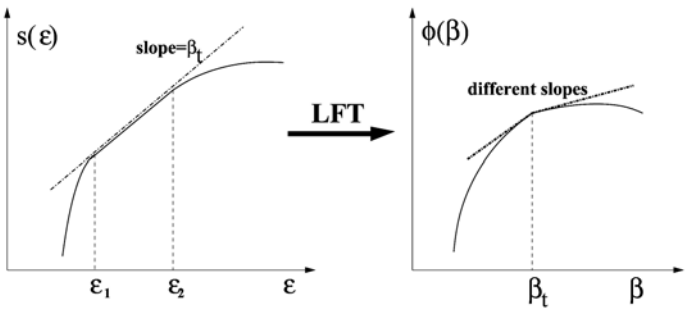

Fig. 12. Relation between entropy and free energy at a first order phase transition.

At a first order phase transition, entropy has a constant slope in the energy range $[\varepsilon_1, \varepsilon_2]$ (the phase coexistence region), resulting into a free energy with a cusp at the transition inverse temperature β_t, see Fig. 12.

A system with a first order phase transition is an extreme case of equivalence, since there is a continuum of microcanonical states with different energy having the same temperature, specific heat is ill defined and one must introduce the concept of latent heat.

If entropy becomes non concave, as shown in Fig. 5, microcanonical and canonical ensemble are not equivalent. The Legendre-Fenchel transform is no more involutive: if applied to the entropy it returns the correct free energy. However, the Legendre-Fenchel transform of the free energy does not coincide with the entropy but rather with its concave envelope. This is the basic feature causing ensemble inequivalence.

As a side remark, let us observe that Maxwell's equal area condition

$$\int_{\varepsilon_1}^{\varepsilon_2} d\varepsilon(\beta(\varepsilon) - \beta_t) = 0 \tag{45}$$

implies (and is a consequence of) free energy continuity at β_t.

In the case of a phase transition with symmetry breaking, entropy can have two branches, a high energy and a low energy one. For instance, for a ferromagnetic system, the high energy paramagnetic phase with magnetization $m = 0$ and the low energy ferromagnetic phase with $m \neq 0$, see Fig. 13. The two branches of the entropy generically cross with two different slopes, i.e. two different temperatures. At a given energy ε_t two different microcanonical temperatures can coexist, we find a temperature jump. This is not conceptually different from the energy jump (latent heat) found in the canonical ensemble. A temperature jump can only appear in an

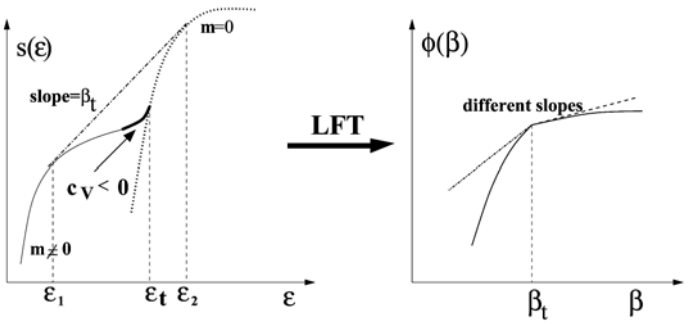

Fig. 13. Left panel: Microcanonical entropy with negative specific heat and temperature jump in a system with symmetry breaking. Right panel: Corresponding free energy in the canonical ensemble.

energy range where entropy is globally convex. In Fig. 13 we show a situation where also a region of negative specific heat is present, but this is not necessary for the existence of a temperature jump. The whole region where these peculiar phenomena appear is completely washed out in the canonical ensemble. As shown in Fig. 13, after Legendre-Fenchel transform, one obtains a free energy which has the same features as the one modeling a first-order phase transition. It has indeed been conjectured that a necessary condition in order to have negative specific heat and temperature jumps in the microcanonical ensemble is the presence of a first-order transition in the canonical ensemble.

In order to better understand the origin of negative specific heat, it is useful to introduce the constrained entropy

$$s(\varepsilon, m) = \lim_{N\to\infty} \frac{\ln \sum_{\{S_i\}} \delta(E - H(\{S_i\}))\delta(Nm - M(\{S_i\}))}{N}\,, \tag{46}$$

where S_i is a discrete spin variable (e.g. $S_i = \pm 1$), $M = \sum_i S_i$ is the extensive magnetization and $m = M/N$ the magnetization per spin. In terms of the constrained entropy, we define the corresponding free energy as

$$\beta f(\beta, \varepsilon, m) = \beta\varepsilon - s(\varepsilon, m)\,. \tag{47}$$

The microcanonical and canonical variational problems can be defined as follows

$$s(\varepsilon) = \sup_m s(\varepsilon, m) \quad , \quad f(\beta) = \inf_{m,\varepsilon} f(\beta, \varepsilon, m)\,. \tag{48}$$

In the canonical extremal problem we seek for values of ε and m that realise an extremum of $f(\beta)$, while in the microcanonical problem we only maximize over m. It can be easily checked that the extrema are the same for the two problems. However,

the stability is different. In the microcanonical problem the only condition for stability is $s_{mm} < 0$ (the subscript mm indicates a double derivative with respect to m), while in the canonical problem the trace and determinant of the Hessian must be positive, implying that $s_{\varepsilon\varepsilon}$ and s_{mm} are both negative and $s_{\varepsilon m}^2 - s_{\varepsilon\varepsilon} s_{mm} > 0$. The canonical problem is more constrained. It can be shown that the specific heat has the following expession in both ensembles

$$c_V = \frac{\beta^2 s_{mm}}{(s_{\varepsilon m}^2 - s_{\varepsilon\varepsilon} s_{mm})} \tag{49}$$

which implies that specific heat is always positive in the canonical ensemble, while it can be negative in the microcanonical ensemble at free energy saddles $s_{\varepsilon\varepsilon} > 0$, $s_{mm} < 0$.

A paradigmatic system showing ensemble inequivalence is the spin-1 Blume-Capel model

$$H_{BC}^N = \Delta \sum_i S_i^2 - \frac{J}{2N} \sum_{i,j} S_i S_j \qquad S_i = 0, \pm 1 \,. \tag{50}$$

The phase diagram in the canonical ensemble shows second and first order phase transitions separated by a tricritical point at $\Delta/J = \ln 4/3, T/J = 1/3$, see Fig. 14. Without loss of generality, one can set $J = 1$. The first order transition at zero temperature is easily located by equating the energies of the ferromagnetic and of the paramagnetic phases: $E_{ferro} = \Delta - 1/2$, $E_{para} = 0$. The second order transition at $\Delta = 0$ is the usual Curie-Weiss transition for a spin one system, obtained by solving the consistency equation $(\exp(\beta m) - \exp(-\beta m))/(\exp(\beta m) + \exp(-\beta m) + 1) = m$.

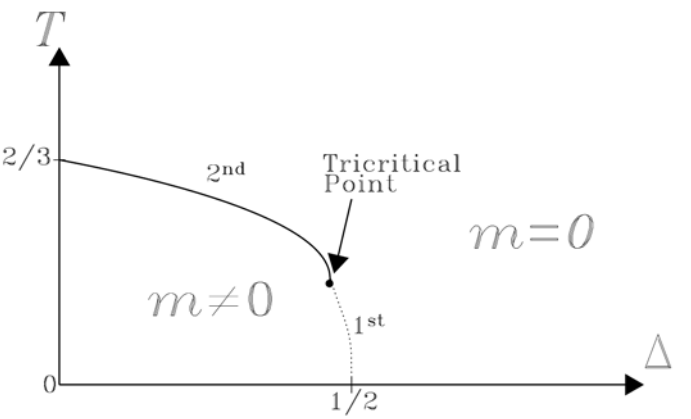

Fig. 14. Phase diagram of the Blume-Capel model (50).

The entropy of the model can be obtained by a direct counting of the number of states. A typical configuration of the model with e.g. $N=30, N_+=11, N_-=9, N_0=10$ is

$$(51) \qquad +++++++----00000---------++0000++$$

Given N_+, N_- and N_0, one can exchange any pair in the group of up, down and zero spins without changing the energy. Therefore the number of configurations with given energy is

$$(52) \qquad \Omega = \frac{N!}{N_+!N_-!N_0!}\,.$$

In the Stirling approximation, $\ln n! = n\ln n - n$, the entropy is

$$(53) \quad S = -k_B N[(1-q)\ln(1-q) + \frac{1}{2}(q+m)\ln\left(\frac{q+m}{2}\right) + \frac{1}{2}(q-m)\ln\left(\frac{q-m}{2}\right)$$

where $m = (N_+ - N_-)/N$ and $q = (N_+ + N_-)/N$. The "quadrupolar moment" q can be expressed in terms of the energy per spin using the relation

$$(54) \qquad \varepsilon = \frac{E}{N} = \Delta(q - Km^2)\,,$$

where $K = J/2\Delta$. Then, by maximizing expression (53) with respect to m at fixed ε one obtains microcanonical entropy. The derivative of this entropy with respect to energy gives inverse temperature. Microcanonical temperature is plotted towards

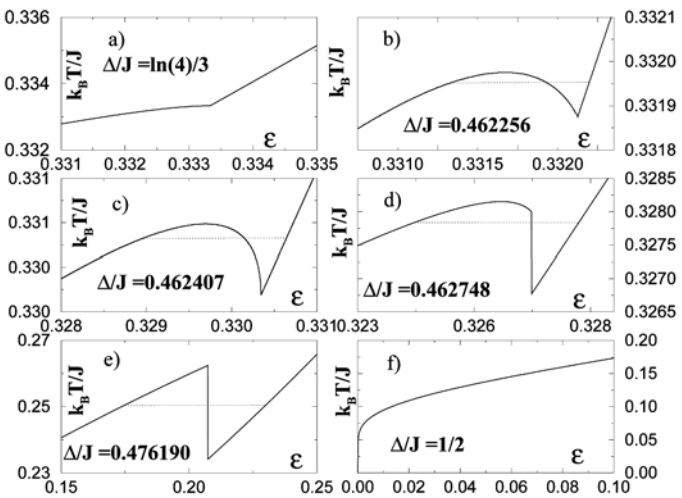

Fig. 15. Temperature versus energy for the Blume-Capel model for different values of Δ/J, showing how negative specific heat and temperature jumps develop when entering the region where the phase transition is first order in the canonical ensemble.

energy in Fig. 15 for decreasing values of Δ/J, starting with the value at the canonical tricritical point in panel a) (for which the derivative of temperature with respect to energy vanishes at the transition energy). Maxwell's constructions are also shown by the horizontal dotted line: they define the canonical transition temperature. A negative specific heat region appears in panel b), as soon as the phase transition becomes first order in the canonical ensemble. At the microcanonical tricritical point (panel c)) the derivative of temperature with respect to energy diverges at the transition energy (specific heat becomes infinitely negative). In panel d) one observes the development of a temperature jump. In panel e) only a temperature jump is present, no negative specific heat. Finally at $\Delta/J = 1/2$ temperature has an infinite slope at zero energy, otherwise the curve is smooth.

The microcanonical tricritical point can be found by expanding the entropy in series of m

$$s = k_B(s_0 + Am^2 + Bm^4 + \dots)\,. \tag{55}$$

The coefficients of the expansion are

$$s_0 = -(1-\varepsilon)\ln(1-\varepsilon) - \varepsilon\ln\varepsilon + \varepsilon\ln 2 \tag{56}$$

$$A = -K\ln\left(\frac{\varepsilon}{2(1-\varepsilon)}\right) - \frac{1}{2\varepsilon} \tag{57}$$

$$B = -\frac{K^2}{2\varepsilon(1-\varepsilon)} + \frac{K}{2\varepsilon^2} - \frac{1}{12\varepsilon^3}\,, \tag{58}$$

where $\varepsilon = \varepsilon/\Delta$. In order to obtain the second order transition line one has to impose that $A = 0$ with $B < 0$. This line coincides with the canonical second order line in Fig. 14. The microcanonical tricritical point is determined by the condition $A = B = 0$. Here is the comparison with the canonical tricritical point

- Canonical $K_{tr} \approx 1.0820$, $\beta_{tr}\Delta = 1.3995$,
- Microcanonical $K_{tr} \approx 1.0813$, $\beta_{tr}\Delta = 1.3998$.

Although these two points are quite close for this model, they do not coincide. For other models the distance between these two points is larger. The region of the phase diagram near the canonical (CTP) and microcanonical (MTP) tricritical points is pictorially represented in Fig. 16. In the microcanonical ensemble, the second-order line continues below CTP (dashed line) and reaches MTP, from there it splits in two lines, a signature of temperature jumps. The two lines join together, and join also the canonical first-order line, at $T = 0$. In the region between the two microcanonical lines one finds only metastable and unstable states of the microcanonical ensemble (coexistence region). This type of pattern of transitions is found in many different models.

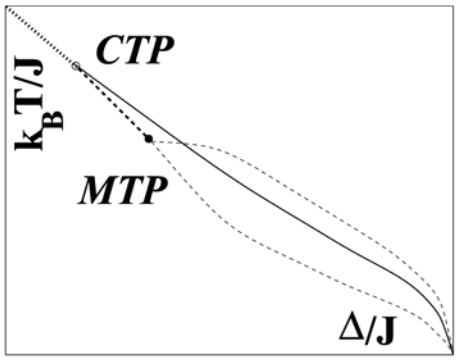

Fig. 16. Zoom of the phase diagram of the Blume-Capel model in the tricritical region. CTP and MTP are the canonical and microcanonical tricritical points, respectively. The dotted line above CTP is the canonical/microcanonical second-order line. The full line is the canonical first-order line.

Coming back to temperature jumps, there is a close relation with Maxwell's constructions in the microcanonical ensemble. This is displayed in Fig. 17, where the $\beta(\varepsilon)$ curve is drawn including metastable (dashed) and unstable (dotted) states. Maxwell's equal area construction is based on the identity

$$\int_{\beta_L^*}^{\beta_H^*} [\varepsilon(\beta) - \varepsilon_t] d\beta = 0 \,, \tag{59}$$

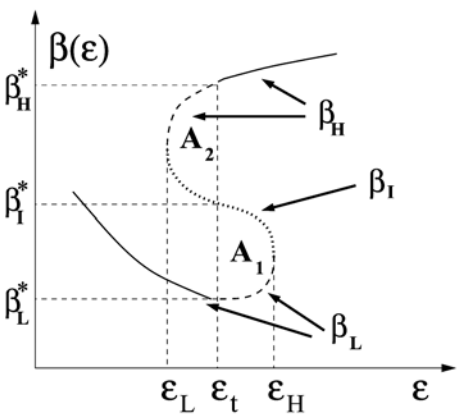

Fig. 17. Inverse microcanonical temperature β vs. energy ε near a temperature jump. Stable states are represented by a full line, metastable by the dashed line and unstable by a dotted line.

which is equivalent to require that microcanonical entropy is a continuous function of ε at ε_t.

An interesting case of ensemble inequivalence is found for the Kardar-Nagel model

$$H_{KN}^N = -\frac{K}{2}\sum_{i=1}^{N}(S_iS_{i+1}-1) - \frac{J}{2N}\left(\sum_{i=1}^{N}S_i\right)^2 . \tag{60}$$

Spins $S_i = \pm 1$ sit on the sites of a one-dimensional lattice and are coupled both nearest-neighbour with strength K and with a Curie-Weiss ferromagnetic ($J > 0$) term. Let $U = -(1/2)\sum_i (S_iS_{i+1}-1)$ be the number of antiferromagnetic bonds in a given configuration characterized by N_+ up spins and N_- down spins, e.g. $N_+ = 12$, $N_- = 8$, $U/2 = 2$

$$++++++|-----|++++|---|++ \tag{61}$$

Simple counting arguments yield to leading order

$$\Omega(N_+, N_-, U) \approx \binom{N_+ - 1}{U/2 - 1}\binom{N_- - 1}{U/2 - 1} . \tag{62}$$

Expressing N_+ and N_- in terms of $N = N_+ + N_-$ and the magnetization $M = N_+ - N_-$, and denoting $m = M/N$, $u = U/N$, one finds that the entropy per spin in the thermodynamic limit is given by

$$\begin{aligned} s(\varepsilon, m) = &\frac{1}{2}(1+m)\ln(1+m) + \frac{1}{2}(1-m)\ln(1-m) \\ &-u\ln u - \frac{1}{2}(1+m-u)\ln(1+m-u) \\ &-\frac{1}{2}(1-m-u)\ln(1-m-u) , \end{aligned}$$

where u satisfies

$$\varepsilon = -\frac{J}{2}m^2 + Ku . \tag{63}$$

By maximizing $s(\varepsilon, m)$ with respect to m one obtains both the spontaneous magnetization $m_s(\varepsilon)$ and the entropy $s(\varepsilon) \equiv s(\varepsilon, m_s(\varepsilon))$ of the system for a given energy. The phase diagram of the model in the (K, T) plane (J is again set to one with no loss of generality) is shown in Fig. 18. As for the Blume-Capel model, the microcanonical and canonical tricritical points do not coincide: $K_{MTP} \simeq -0.359, K_{CTP} = -\ln 3/2\sqrt{3} \simeq -0.317$. The interesting parameter region is the one with K negative, because the local antiferromagnetic interaction

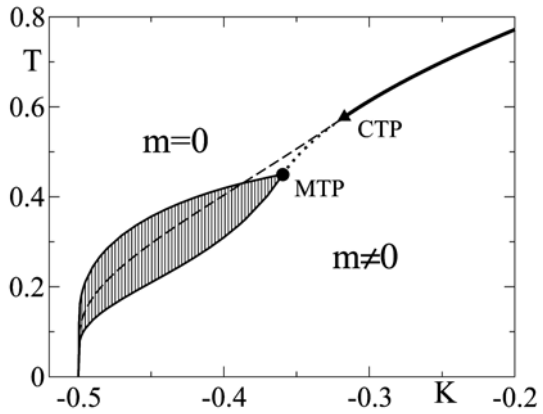

Fig. 18. Phase diagram of the Kardar-Nagel model. In the canonical ensemble the large K transition is continuous (bold solid line) down to the tricritical point CTP where it becomes first order (dashed line). In the microcanonical ensemble the continuous transition coincides with the canonical one at large K (bold line). It persists at lower K (dotted line) down to the tricritical point MTP where it turns first order, with a branching of the transition line (solid lines). The region between these two lines (shaded area) is not accessible in the microcanonical ensemble.

compete with the global ferromagnetic one. Let us further remark that the transition at $T = 0$ can be obtained by imposing that the state with alternating down and up spins $+-+-+-\cdots$ has the same energy as the ferromagnetic state $+++++\cdots$.

A phenomenon which has been first studied for the Kardar-Nagel model is broken ergodicity. This is expected because of the non convexity of the region of macroscopic accessible states, see Fig. 3, which is a direct consequence of non additivity. Let us consider positive magnetizations states, hence $N_+ > N_-$. Then $0 < U < 2N_- = N - M$, the left bound corresponding to configurations where all down spins are isolated

$$+++++|-|+++|-|++++|-|+++++ \tag{64}$$

This in turn implies, in the $N \to \infty$ limit,

$$0 \leq u = \frac{\varepsilon}{K} + \frac{J}{2K} m^2 \leq 1 - m. \tag{65}$$

As a consequence, the allowed magnetization/energy states are those within the shaded area in Fig. 19. From this figure, it is evident that there are energies (for instance $\varepsilon = -0.35$) for which magnetization admits values within three different intervals: one around $m = 0$ and two around opposite values of m. Any continuous

energy conserving dynamics started in one of these intervals cannot allow for a

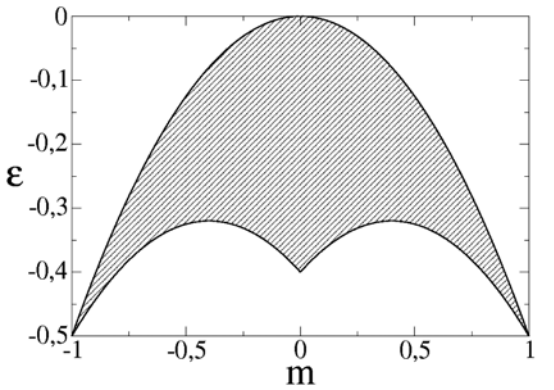

Fig. 19. Allowed magnetization/energy states for model (60) for $K = -0.4$ and $J = 1$.

transition to states belonging to another interval. Therefore ergodicity on the energy surface is broken. An example is shown in Fig. 20. In the upper panel, the system is run at an energy, $\varepsilon = -0.318$, for which the energy surface is connected and the system is ergodic. Nevertheless, the magnetization jumps among the three

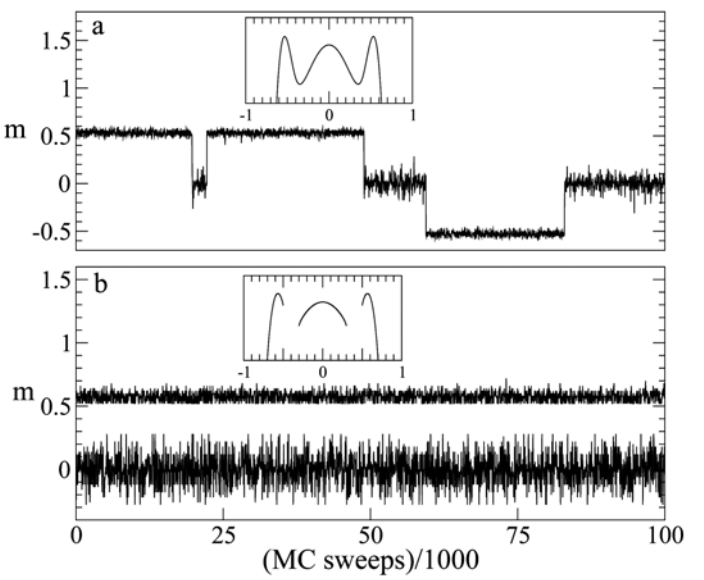

Fig. 20. Microcanonical Montecarlo simulation of the Kardar-Nagel model (60) with $K = -0.4$ and $J = 1$ at different energies, showing ergodicity breaking (lower panel).

maxima of the entropy (shown in the inset). In the lower panel, the energy is $\varepsilon = -0.325$ and the accessible values of the magnetization are splitted into three intervals. Therefore, if magnetization is started around zero, its value remains around zero forever, as shown in one of the time series. In the other, magnetization remains at a positive value. No transition among these states is possible. Entropy, shown in the insets, has gaps, corresponding to regions where the density of states is zero.

Let us briefly recall how to simulate the microcanonical ensemble using Creutz's algorithm. In this algorithm one probes the microstates of the system with energy $\leq E$. This is implemented by adding an auxiliary variable, called the "demon", such that

$$E_S + E_D = E\,, \tag{66}$$

with $E_D > 0$. The simulation begins with $E_S = E, E_D = 0$ and attempt a spin flip. The move is accepted if the energy decreases. The excess energy is given to the demon

$$E_S \to E_S - \Delta E \quad , \quad E_D \to E_D + \Delta E \quad , \quad \Delta E > 0\,. \tag{67}$$

If instead the energy increases, the energy needed is taken from the demon

$$E_S \to E_S + \Delta E \quad , \quad E_D \to E_D - \Delta E \quad , \quad \Delta E > 0\,. \tag{68}$$

One rejects the move if the demon does not have the needed energy, but one keeps the configuration in the computation of averages. It can be proven that this dynamics respects detailed balance and that the microcanonical measure (all configurations have equal weight on the energy surface) is stationary. One can also prove that the probability distribution of the demon energy is exponential

$$p(E_D) \propto \exp(-\beta E_D) \tag{69}$$

and use this property to determine microcanonical inverse temperature β.

3 - Large Deviation Theory

In this Section we will show how large deviation theory can be used to compute the entropy of long-range systems within the microcanonical ensemble. We begin by recalling what is large deviation theory about.

Let us consider a set of N d-dimensional random variables $\mathbf{X}_i$, $i = 1, \ldots, N$, $\mathbf{X}_i \in \mathbb{R}^d$, whose probability distribution function (PDF) is $p(\{\mathbf{X}_i\})$.

In large deviation theory, one is interested in deriving the PDF of extensive observable, in particular the sample mean, defined as

$$\mathbf{M}_N = \frac{1}{N}\sum_{i=1}^{N} \mathbf{X}_i\,, \tag{70}$$

in the limit of large N.

A *large deviation principle* is formulated, according to which the following limit exists

$$I(x) = \lim_{N\to\infty} -\frac{1}{N} \ln P(\mathbf{M}_N \in [x, x+dx]) \,, \tag{71}$$

and defines the rate function $I(x)$. This means that, at leading order, $P(\mathbf{M}_N \in [x, x+dx]) \sim \exp(-NI(x))$.

Let us define the scaled cumulant generating function (SCGF)

$$\psi(\lambda) = \lim_{N\to\infty} \frac{1}{N} \ln \mathbb{E}\left[\exp\left(\lambda \sum_{i=1}^{N} \mathbf{X}_i\right)\right] \tag{72}$$

where $\lambda \in \mathbb{R}^d$ and the average $\mathbb{E}[]$ is performed over the PDF of $\mathbf{X}_i$. Gartner-Ellis' theorem states that the rate function is

$$I(x) = \sup_{\lambda\in\mathbb{R}^d} \{\lambda x - \psi(\lambda)\} \tag{73}$$

when $\psi(\lambda) < \infty$ and is differentiable everywhere. If the random variables $\mathbf{X}_i$ are independent and identically distributed (i.i.d.) the SCGF is differentiable and assumes the form

$$\psi(\lambda) = \ln \langle \exp(\lambda \mathbf{X}) \rangle \tag{74}$$

where $\langle\,\rangle$ is the average with respect to the distribution of the single variable.

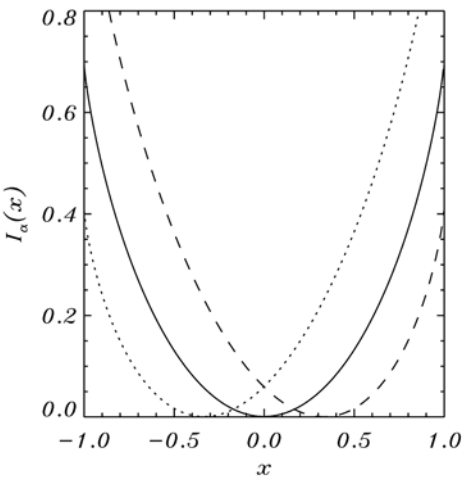

Fig. 21. The rate function of biased coin tossing for $\alpha = 1/3$ (long-dashed), $1/2$ (full), $2/3$ (short-dashed).

Let us consider the example of biased coin tossing, which physically corresponds to a model of non-interacting spins. The i.i.d. random variables $\mathbf{X}_i$ take the value -1 with probability α and $+1$ with probability $1-\alpha$, with $\alpha \in [0,1]$. The SCGF is

$$\psi_\alpha(\lambda) = \ln\{\exp(\lambda) - 2\alpha\sinh(\lambda)\}\,. \tag{75}$$

When $\alpha = 1/2$ coin tossing is unbiased. In Fig. 21 we show the rate function for $\alpha = 1/3, 1/2, 2/3$.

Let us now come to discuss the relevance of these results for statistical mechanics. In the statistical mechanics vocabulary the rate function $I(x)$ corresponds to the opposite of Boltzmann entropy of a macrostate characterized by a fraction x of up-spins. More generally, and not necessarily with reference to spin systems, thermodynamic functions, such as microcanonical entropy and free energy, can be computed using large deviations theory. Let us briefly illustrate this approach.

The first step is to express the Hamiltonian of the system in terms of global variables γ

$$H_N(\omega_N) = \widetilde{H}_N(\gamma(\omega_N)) + R_N(\omega_N) \tag{76}$$

where ω_N is a phase-space configuration of the N particles and R_N is a sub-extensive rest of the full Hamiltonian of the system. Global variables play the role of the observables for which we compute the PDF. Hence, we are naturally led to take the following limit of infinite number particles

$$h(\gamma) = \lim_{N\to\infty} \frac{H_N}{N} = \lim_{N\to\infty} \frac{\widetilde{H}_N}{N}\,. \tag{77}$$

The second step is to compute the entropy in terms of the global variables

$$s(\gamma) = \lim_{N\to\infty} \frac{1}{N} \ln \Omega_N(\gamma) \tag{78}$$

where $\Omega(\gamma)$ is the number of microscopic configurations ω_N with a fixed value of γ. It turns out that the entropy is the opposite of the rate function.

The third step is to solve either the microcanonical

$$s(\varepsilon) = \sup_\gamma \{s(\gamma) | h(\gamma) = \varepsilon\} \tag{79}$$

or the canonical

$$\beta f(\beta) = \inf_\gamma \{\beta h(\gamma) - s(\gamma)\} \tag{80}$$

variational problem. Free energy (80) is the Legendre-Fenchel transform of microcanonical entropy (79). On the other hand, the Legendre-Fenchel transform of free energy is not microcanonical entropy, but rather its concave envelope. When the

concave envelope coincides with microcanonical entropy, the two ensembles are equivalent.

In order to illustrate this solution method on a concrete example, we consider the mean-field three-state Potts model. Its Hamiltonian takes the form

$$H^N_{Potts} = -\frac{J}{N}\sum_{i,j=1}^{N}\delta_{S_i,S_j}\,, \tag{81}$$

where at every lattice site i we associate a spin variable $S_i = a, b, c$ and δ is Kronecker's δ-symbol. We identify the spins as the local random variables. The first step of the procedure consists in the identification of the global variables. The form and the symmetries of the Hamiltonian suggest to define the following vector

$$\gamma = (n_a, n_b, n_c) \tag{82}$$

where

$$n_\alpha = \frac{1}{N}\sum_i \delta_{S_i,\alpha}, \quad \alpha = a, b, c \tag{83}$$

represents the fraction of local random variables populating a given state α. Using these global variables, the Hamiltonian reads

$$\widetilde{H}^{Potts}_N = -\frac{JN}{2}(n_a^2 + n_b^2 + n_c^2) = Nh(\gamma)\,. \tag{84}$$

The second step consists in the calculation of entropy in terms of the global variables. Assuming that the three values of the local random variable are equally probable (this corresponds to the principle of "maximal ignorance" often used in statistical mechanics), the SCGF is

$$\begin{aligned}\psi(\lambda) &= \ln\left(\frac{1}{3}\sum_{S=a,b,c}\left(e^{\lambda_a\delta_{S,a}} + e^{\lambda_b\delta_{S,b}} + e^{\lambda_c\delta_{S,c}}\right)\right)\\ &= \ln\left(\frac{1}{3}\left(e^{\lambda_a} + e^{\lambda_b} + e^{\lambda_c}\right)\right)\end{aligned}$$

where $\lambda = (\lambda_a, \lambda_b, \lambda_c)$ are Lagrange mulipliers. The corresponding rate function is then given by formula (73)

$$I(\gamma) = \sup_\lambda\{\lambda_a n_a + \lambda_b n_b + \lambda_c n_c - \psi(\lambda)\}\,. \tag{85}$$

The extrema of the bracketed expression are $\lambda_\alpha = \ln n_\alpha$, with $\alpha = a, b, c$. Entropy, as a function of the global variables, is then

$$s(\gamma) = -I(\gamma) + \ln\mathcal{N} \tag{86}$$

where the term $\ln \mathcal{N}$ derives from the normalization of the probability, and in this case is $\ln \mathcal{N} = \ln 3$.

In the third step one evaluates microcanonical entropy from the variational formula

$$s(\varepsilon) = \sup_{n_a, n_b} \left\{ - n_a \ln n_a - n_b \ln n_b - (1 - n_a - n_b) \ln (1 - n_a - n_b) \middle| h(n_a, n_b) = \varepsilon \right\}. \tag{87}$$

The solution of this variational problem is necessarily numerical, because it implies the solution of an implicit equation. However, both the derivation of entropy and of microcanonical temperature is straightforward. The dependence of microcanonical temperature on energy is shown in Fig. 22: it has a parabolic shape and in the energy range where β grows, $[-0.215\,J, -J/6]$, specific heat is negative. By solving the canonical variational problem

$$\beta f(\beta) = \inf_{n_a, n_b, n_c} \left\{ \sum_{\alpha} n_\alpha \ln n_\alpha - \frac{\beta J}{2} (n_a^2 + n_b^2 + n_c^2) \right\} \tag{88}$$

one can get the average energy ε as a function of β from $\varepsilon = \partial(\beta f)/\partial\beta$. This curve is also plotted in Fig. 22. It coincides with the microcanonical curve for energies below $\varepsilon^t = -0.255\,J$. At the inverse temperature value $\beta^t = 2.75$ the model undergoes a

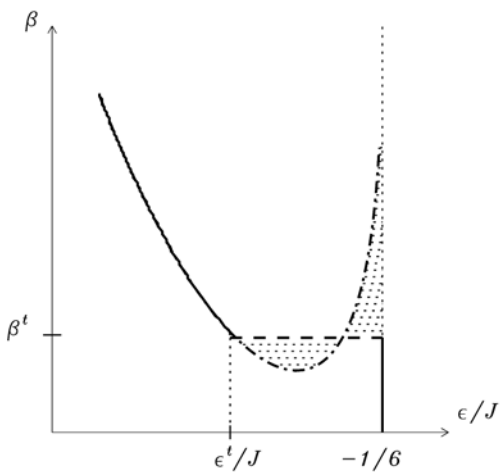

Fig. 22. Inverse temperature vs. energy for the mean-field three-state Potts model in both the microcanonical and the canonical ensemble. The microcanonical solution coincides with the canonical one for $\varepsilon \leq \varepsilon^t$ and is otherwise shown by the dash-dotted line for $\varepsilon^t \leq \varepsilon < -J/6$. The increasing part of the microcanonical dash-dotted line corresponds to a negative specific heat region. In the canonical ensemble, the model displays a first order phase transition at β^t. The two dotted regions bounded by the dashed line and by the microcanonical dash-dotted line have the same area, corresponding to a Maxwell's construction.

first order phase transition, with an associated latent heat. Hence, the results are quite different in the two ensembles: a first order phase transition in the canonical ensemble and no phase transition in the microcanonical ensemble with an associated negative specific heat region in energy. We will now deal with a model whose Hamiltonian depends on continuous variable, to show the efficiency of the large deviation method also for this case. It's evident that the calculation of the density of states by direct counting is not viable for such models. Let us consider the following Hamiltonian, which describes the motion of N XY spins on a fully connected lattice

$$H_{XY} = \sum_{i=1}^{N} \frac{p_i^2}{2} - \frac{J}{2N}\left(\sum_i \vec{s}_i\right)^2 - \frac{K}{4N^3}\left[\left(\sum_i \vec{s}_i\right)^2\right]^2 , \tag{89}$$

where $\vec{s}_i = (\cos\theta_i, \sin\theta_i)$ is a spin vector with constant modulus and direction $\theta_i \in [-\pi, \pi]$. The local variable p_i is the conjugated momentum of the angle θ_i. The two coupling constants J and K are scaled differently: the first one by $1/N$ following Kac's prescription and the second one by $1/N^3$, in order to make the contribution of the last term of the same size as the others in the $N \to \infty$ limit. For $K = 0$ the model reduces to the HMF model, which we will discuss in the next Section. We will here sketch how to get microcanonical entropy using the large deviation approach. The three steps procedure begins with the identification of the global variables. For this model, it is natural to choose $\mathbf{X} = (\cos\theta, \sin\theta, p^2)$ as the random local variable. We then define magnetization along the X and the Y directions as

$$m_x = \frac{1}{N}\sum_i \cos\theta_i, \quad m_y = \frac{1}{N}\sum_i \sin\theta_i \tag{90}$$

and the corresponding magnetization vector $\mathbf{m} = (m_x, m_y)$, which is the order parameter of the paramagnetic-ferromagnetic phase transition taking place in this model. Using the two components of magnetization and the average kinetic energy $E_K = \sum_i p_i^2/N$, we define the three dimensional vector of global variables as

$$\gamma = (m_x, m_y, E_K)\,. \tag{91}$$

In terms of the global variables, energy density can be written as

$$h(\gamma) = \frac{1}{2}\left(E_K - Jm^2 - \frac{K}{2}m^4\right). \tag{92}$$

The SCGF is given at leading order by

$$\psi(\lambda) \simeq \ln\left[\frac{I_0\left(\sqrt{\lambda_x^2 + \lambda_y^2}\right)}{\sqrt{-\lambda_K}}\right], \tag{93}$$

where I_0 is the modified Bessel function of order zero and $\lambda_x, \lambda_y, \lambda_K$ are Lagrange multipliers. The corresponding rate function, which depends on the global variables, is evaluated by using formula (73). From the rate function, which is nothing but the opposite of entropy, function of the global variables, one can again obtain microcanonical entropy solving a variational problem. Similarly, for canonical free energy.

Let us summarize the main features of this model. Varying the value of the ratio between the coupling constants $K \geq 0$ and $J > 0$ the system shows different behaviours. We have already mentioned that for $K = 0$ the model reduces to the HMF model. This latter has a second order phase transition at $T/J = 1/2$. Ensembles are equivalent in this limit. The second order transition extends to $K > 0$ for both the canonical and the microcanonical ensemble, see Fig. 23. The canonical second order line remains at the temperature $T/J = 0.5$ along the segment with $K/J \in [0, 0.5)$. At $K/J = 0.5$, $T/J = 0.5$ there is a canonical tricritical point. For larger values of K/J the predictions of the two ensembles differ. In the canonical ensemble the transition become first order, see the upper dotted line in Fig. 23. In the microcanonical ensemble the line remains of second order with constant value of the temperature $T/J = 0.5$, up to the microcanonical tricritical point at $K/J = 5/2$. Between the canonical first order line and the microcanonical

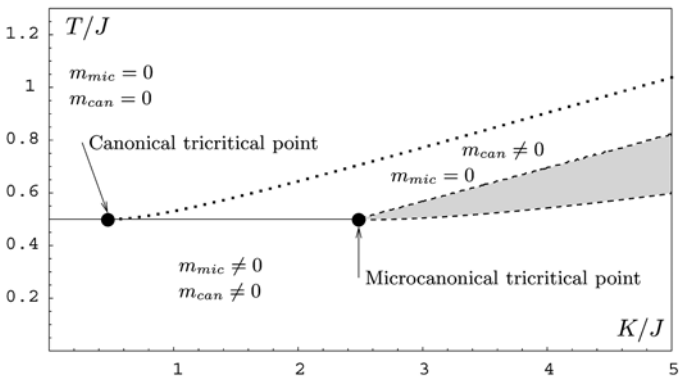

Fig. 23. Phase diagram of the XY model (89) for both the canonical and microcanonical ensemble.The canonical second order transition line (solid line at $T/J = 1/2$) becomes first order (dotted line, determined numerically) at the canonical tricritical point. The microcanonical second order transition line coincides with the canonical one below $K/J = 1/2$ but extends further to the right up to the microcanonical tricritical point at $K/J = 5/2$. At this latter point, the transition line bifurcates in two first order microcanonical lines, corresponding to a temperature jump. The region within these lines is forbidden in the microcanonical ensemble. In the figure we also report the magnetization in the different parts of the diagram.

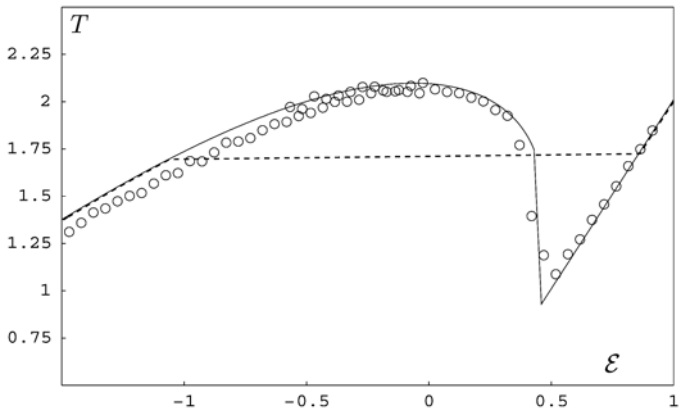

Fig. 24. Caloric curve for the XY model (89) with $K/J = 10$. The solid line is the theoretical prediction in the microcanonical ensemble. It shows a phase transition where temperature has a jump. A negative specific heat region is present, where temperature has a negative slope. The points correspond to the results of molecular dynamics simulations of a system composed by $N = 100$ spins. The transition is smooth due to finite size effects. The dashed line represents the first order phase transition in the canonical ensemble.

second order line the ensembles give different predictions for the order parameter, which is zero (paramagnetic phase) in the microcanonical ensemble and non zero (ferromagnetic phase) in the canonical ensemble. Increasing the coupling, $K/J > 5/2$, the difference between the predictions of the two ensembles becomes even more peculiar. While in the canonical ensemble the transition remains first order, in the microcanonical ensemble, temperature jumps appear. The coexistence of two temperatures at the transition energy is shown by the two dotted lines in Fig. 23. No stable microcanonical states exist between the two lines. Fig. 24 shows the caloric curve for $K/J = 10$: both a region of negative specific heat and a temperature jump are presents in the microcanonical ensemble. We consider now the case $J = -1$ and $K > 0$. With these values of the coupling constants there is a competition between a ferromagnetic and an anti-ferromagnetic term in the Hamiltonian. Intuitively, we expect that for large values of $|K/J|$ the system is ferromagnetic, while for small values of this ratio the anti-ferromagnetic term dominates and the system becomes paramagnetic for all energies. For some intermediate values of this ratio, the system shows a phase transition between a paramagnetic and a ferromagnetic phase. In both these phases, due to the competition, there are gaps in the accessible values of magnetization at a fixed energy. This produces a lack of ergodicity, as already discussed in Section 2 for the Kardar-Nagel model. A convenient parameter plane

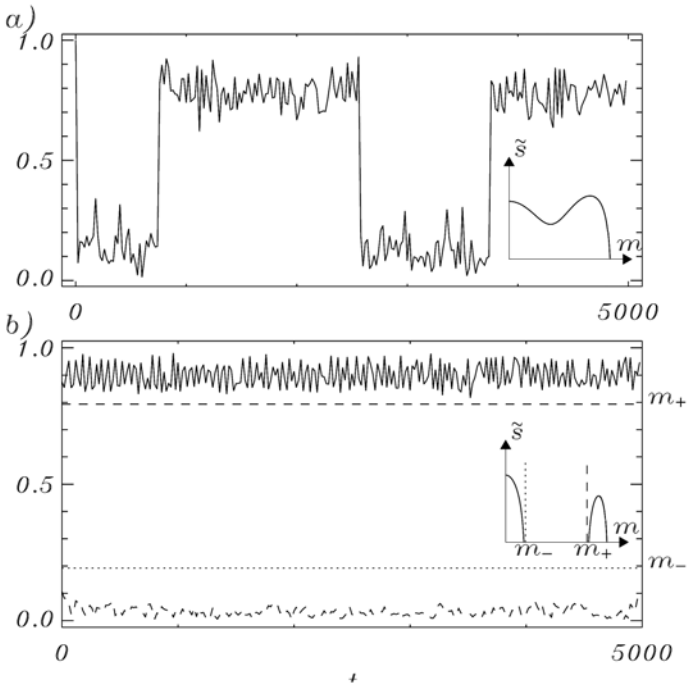

Fig. 25. Time evolution of the magnetization for the XY model (89) with $J = -1$. Panel a) corresponds to the case $\varepsilon = 0.1$, $K = 8$, panel b) to $\varepsilon = 0.0177$, $K = 3$. In panel a) magnetization flips from a value close to zero to a non zero value, showing that phase space is connected. The corresponding entropy vs. magnetization curve is shown in the inset: it has, as expected, a double hump. In panel b) two different trajectories, started at initially different values of the magnetization, are shown. No flip is observed over a very long time stretch, proving that phase space is indeed disconnected. This is confirmed by the shape of the entropy in the inset, which shows that no accessible macrostate is present in the interval $[m_-, m_+]$.

where to discuss ergodicity breaking for this model is (ε, K). Depending on the values of these two parameters, one may either find a connected phase space or a disconnected one. This is shown in Fig. 25.

In Section 2 we have discussed the solution of the Blume-Capel (50) using standard counting arguments. We want to show here how to obtain that solution using the large deviations procedure we have introduced. The local random variables are the spins $\mathbf{X}_i = (S_i^2, S_i)$, where $S_i = 0, \pm 1$. The identification of the global variables is direct, they are magnetization m and quadrupolar moment q. In terms of the global variables, the Hamiltonian is

$$h(\gamma) = \Delta(q - Km^2)\,. \tag{94}$$

The SCGF is also easily computed

$$\psi(\lambda,\rho) = \ln\langle \exp\{\lambda S^2 + \rho S\}\rangle = \ln\left(1 + 2e^{\lambda}\cosh(\rho)\right) - \ln 3\,, \tag{95}$$

where λ and ρ are Lagrange multipliers. The rate function then reads

$$I(\gamma) = \sup_{\lambda,\rho}\{\rho m + \lambda q - \psi(\lambda,\rho)\} \tag{96}$$

and the solution of this variational problem gives

$$\rho = \tanh^{-1}(q/m) \quad , \quad \lambda = -\ln\left(2\cosh(\rho(q,m))\right) + \ln\left(m/(1-m)\right). \tag{97}$$

The substitution of these values into (96) returns the rate function in terms of the global variables. Finally, the computation of the supremum of the rate function with fixed energy gives us microcanonical entropy, which turns out to be the same of formula (53). Hence, the use of large deviation method is a valid alternative to the direct counting method, which is not always viable.

The free electron laser model (43) introduced in Section 2 can also be solved using the large deviation method. The global variables are $\gamma = (m, A, \sigma)$, where m is magnetization, A is the modulus of the field and

$$\sigma = \frac{1}{N}\sum_i p_i + A^2 \tag{98}$$

total momentum. Using the same three steps procedure described above, the microcanonical entropy is obtained by solving the following variational problem

$$s(\varepsilon,\sigma,\delta) = \sup_{A,m}\left\{\frac{1}{2}\ln\left[\left(\varepsilon - \frac{\sigma^2}{2}\right) + 4Am + 2(\delta-\sigma)A^2 - A^4\right] + s_{conf}(m)\right\} \tag{99}$$

where the configurational entropy $s_{con}(m)$ is given by

$$s_{conf}(m) = -\sup_{\lambda}\{\lambda m - \ln I_0(\lambda)\} \tag{100}$$

and I_0 is the modified Bessel function of order zero. The model display, a second order phase transition at the critical energy $\varepsilon_c = -1/(2\delta)$ for $\delta < 0$. The microcanonical and canonical ensembles are equivalent.

Ensemble inequivalence can also determine a negative magnetic susceptibility. This quantity is positively defined in the canonical ensemble, but can be negative in the microcanonical ensemble. Let us recall the first law of thermodynamics for magnetic systems, $TdS = dE - hdM$. This formula can be a guide for the interpretation of the formula that allows to define the field h in terms of magnetization m in the microcanonical ensemble

$$h(\varepsilon,m) = -\frac{\partial s}{\partial m}\Big/\frac{\partial s}{\partial \varepsilon} = -\frac{1}{\beta(\varepsilon,m)}\frac{\partial s}{\partial m}\,. \tag{101}$$

In the canonical ensemble

$$f(\beta,h)=\inf_{\varepsilon,m}\left[\varepsilon-hm-\frac{1}{\beta}s(\varepsilon,m)\right] \tag{102}$$

which gives $\partial s/\partial m=-hm$, $\partial s/\partial\varepsilon=\beta$, in agreement with the microcanonical expressions for h and β. The formula for susceptibility is the same in both ensembles, as for specific heat, see (49)

$$\chi=\frac{\partial m}{\partial h}=\beta\frac{s_{\varepsilon\varepsilon}}{s_{\varepsilon m}^2-s_{\varepsilon\varepsilon}s_{mm}}\,. \tag{103}$$

In the canonical ensemble $s_{\varepsilon\varepsilon}>0$ and the denominator is positive as a consequence of stationarity, hence $\chi>0$. In the microcanonical ensemble $s_{mm}<0$ and, at free energy saddles, $s_{\varepsilon\varepsilon}<0$, hence susceptibility can be negative.

To illustrate the concept of negative susceptibility on a concrete example, let us introduce the ϕ^4 mean-field model, which is in the same universality class of the Curie-Weiss model of magnetism

$$H_\phi^N=\sum_i\left(\frac{p_i^2}{2}-\frac{1}{4}q_i^2+\frac{1}{4}q_i^4\right)-\frac{1}{4N}\sum_{i,j}q_iq_j \tag{104}$$

where (q_i,p_i) are conjugate variables. The global variables are

$$m=\frac{1}{N}\sum_i q_i,\quad z=\frac{1}{4N}\sum_i q_i^4-q_i^2,\quad u=\sum_i p_i^2\,. \tag{105}$$

The quantity m corresponds to the magnetization of the system and z is related to the nature of the short-range potential. The SCGF reads

$$\psi(\lambda)=-\frac{\ln\lambda_u}{2}+\ln\int dq\,e^{-\lambda_m q-\lambda_z(q^4-q^2)}+\text{const}\,. \tag{106}$$

Microcanonical entropy in terms of global variables is

$$s(u,z,m)=\inf_{\lambda_u,\lambda_z,\lambda_m}\left\{\lambda_u u+\lambda_z z+\lambda_m m-\psi(\lambda)\right\}, \tag{107}$$

and in terms of energy and magnetization

$$s(\varepsilon,m)=\sup_{u,z}\left(s(u,z,m)|\varepsilon=\frac{u}{2}+z-\frac{m^2}{4}\right). \tag{108}$$

Although this function cannot be obtained in explicit form, because as usual the full analytical treatment implies the solution of an implicit equation, it can be obtained numerically with any precision. Using then formula (103) one obtains an explicit

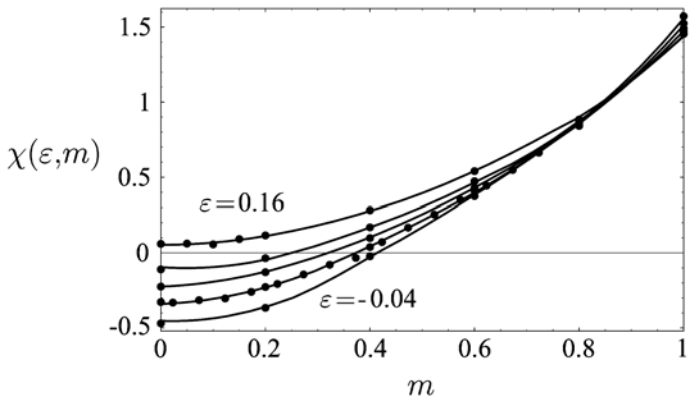

Fig. 26. Susceptibility vs. magnetization for different energies for the ϕ^4 model (104). The full lines are theoretical results, while the points are the results of numerical simulations.

expression of susceptibility for the ϕ^4 model. Fig. 26 shows a comparison of this formula with the numerical results obtained directly from Hamiltonian (104). Below a given energy value, corresponding to the ferromagnetic transition, a range of m appears where susceptibility becomes negative.

When the method described above cannot be used, for instance it is not easy to identify the global variables, one can rely on a procedure that we have called *min-max*. The method begins with an assumption, that the canonical partition function can be written in the following form

$$Z(\beta, N) = \int dx \exp\{-NG(\beta, x)\} \tag{109}$$

with G a differentiable function of β and x, a dummy variable. This is for instance the form that Z takes as a result of a Hubbard-Stratonovich transformation of the Hamiltonian. The free energy is defined as $\phi(\beta) = \beta f(\beta) = \inf_x G(\beta, x)$. Let us introduce the Legendre-Fenchel transform of G by the relation $s(\varepsilon, x) = \inf_\beta \{\beta\varepsilon - G(\beta, x)\}$. Then one can prove that

$$s(\varepsilon) = \sup_x \{s(\varepsilon, x)\} = \sup_x \inf_\beta \{\beta\varepsilon - G(\beta, x)\}\,. \tag{110}$$

Inverting the inf with the sup one gets the concave envelope of $s(\varepsilon)$

$$s^*(\varepsilon) = \inf_\beta \sup_x \{\beta\varepsilon - G(\beta, x)\}\,. \tag{111}$$

On the other hand the Legendre-Fenchel transform of both $s(\varepsilon)$ and $s^*(\varepsilon)$ returns the free energy $\phi(\beta)$. Indeed $\sup\inf \leq \inf\sup$ and the equality holds when the function G is differentiable in both the arguments.

The XY model with both long and short-range interactions

$$H_{SL}^{N} = \sum_i \frac{p_i^2}{2} + \frac{J}{2N}\sum_{i,j}[1-\cos(\theta_i-\theta_j)] - K\sum_i \cos(\theta_{i+1}-\theta_i) \tag{112}$$

can be solved using the min-max method.

The partition function, after an Hubbard-Stratonovich transformation, takes the form

$$Z \sim \int z dz \prod_i d\theta_i \exp\left(-\frac{N\beta}{2}z^2 + \beta z\sum_i \cos\theta_i + \beta K\sum_i \cos(\theta_{i+1}-\theta_i)\right). \tag{113}$$

The integral over the θ_i can be performed using the transfer operator method

$$\mathcal{T}\psi(\theta) = \int d\alpha \exp\left(\beta\frac{z}{2}(\cos\theta+\cos\alpha) + \beta K\cos(\theta-\alpha)\right)\psi(\alpha) \tag{114}$$

and the partition function become

$$Z = \int z dz \exp\left(-\frac{N\beta}{2}z^2 + N\ln\lambda(\beta z,\beta K)\right), \tag{115}$$

where $\lambda(\beta z,\beta K)$ is the largest eigenvalue of the transfer operator $\mathcal{T}$. Entropy is then obtained using the min-max method

$$s(\varepsilon) = \sup_z \inf_\beta \left[\beta u - \beta\frac{1+z^2}{2} + \ln\lambda(\beta z,\beta K) + \frac{1}{2}\ln\frac{2\pi}{\beta}\right]. \tag{116}$$

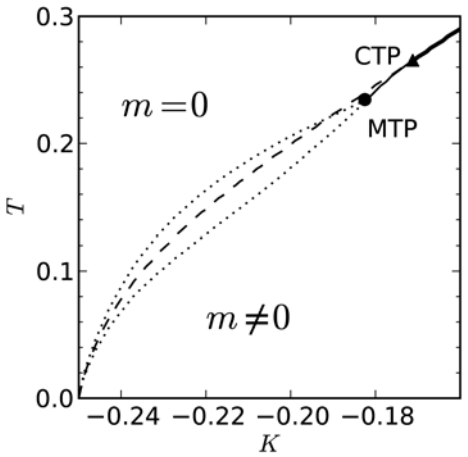

Fig. 27. Phase diagram of the XY model with long and short-range interactions. The full line is the second order line for both the canonical and microcanonical ensemble. The triangular point corresponds to the canonical tricritical point. Below it, the dashed line is the first order transition line in the canonical ensemble. The circular point is the microcanonical tricritical point and the two dotted lines correspond to temperature jumps.

Fig. 27 shows the phase diagram of this model. It is extremely similar to the phase diagram of the Kardar-Nagel model, Fig. 18, hence it can be discussed exactly in the same way. Both the canonical and microcanonical ensemble predict a second order transition line for large T and K, till the canonical tricritical point is reached. Below it, the two ensembles are inequivalent. The canonical ensemble shows a first order transition line, while the microcanonical ensemble predicts a second order line until the microcanonical tricritical point is reached. Here, the latter ensemble shows temperature jumps.

4 - Quasistationary states

Let us consider the Hamiltonian

$$H^N_{HMF} = \sum_{i=1}^{N} \frac{p_i^2}{2} + \frac{1}{2N} \sum_{i,j=1}^{N} (1 - \cos(\theta_i - \theta_j)) . \tag{117}$$

It represents a system of particles moving on the circle, see Fig. 28. Particle i has position θ_i and momentum p_i. They are all coupled with the same strength through a cosine potential. The coupling is scaled by $1/N$, following Kac's prescription, in order to allow kinetic energy to compete with potential energy. In an alternative interpretation, Hamiltonian (117) represents a system of fully coupled XY spins. This model is the $K = 0$ limit of model (112) and of model (89). The model has a low energy phase where potential energy dominates over kinetic energy and particles are clustered. The clustering coefficient is the two component XY "magnetization"

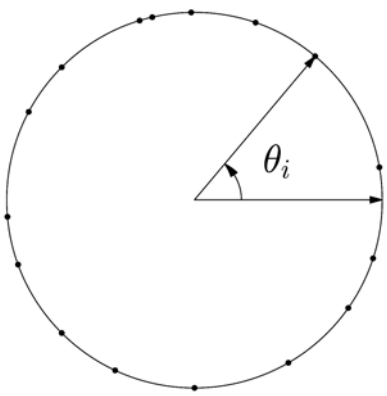

Fig. 28. In the HMF model, particles move on a circle and have positions θ_i.

$\mathbf{m} = (m_x, m_y)$ introduced in (90). The modulus of this vector, m, is non zero in the clustered phase and reaches one at the ground state energy $E = 0$ when all particles collapse to a point on the circle. At high energy, the system is dominated by kinetic energy and the particles homogeneously distribute on the circle: the modulus of magnetization vanishes. The system undergoes a second order phase transition, i.e. magnetization vanishes with continuity. The critical energy of the transition is $\varepsilon_c = 3/4$ and the critical temperature $T_c = 1/2$. In Fig. 29 we plot in the lower panel the caloric curve of the model, the temperature/energy relation, which is nonlinear below the critical energy and linear above. The caloric curve has a kink at the transition energy. Magnetization vs. energy is plotted in the upper panel. Microcanonical and canonical ensemble are equivalent for this model. A feature emerged in the simulation of this model, which then led to the discovery of *quasistationary states*. It was found that for some initial conditions the temperature was not in agreement with the theoretical curve. This is shown in the inset of the lower panel of Fig. 29. Moreover,

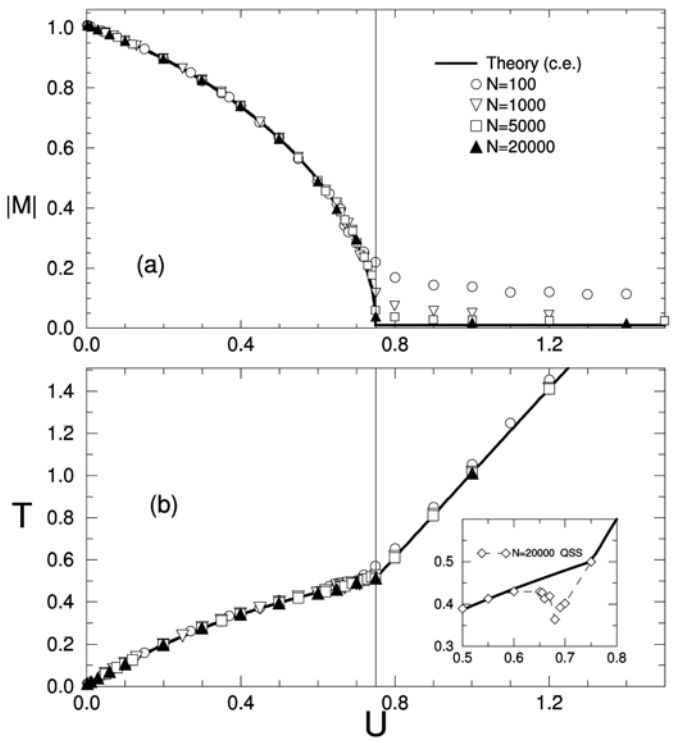

Fig. 29. Lower panel: Caloric curve of the HMF model (117). Upper panel: magnetization vs. energy. The points are the results of numerical simulations, the full lines are obtained analytically.

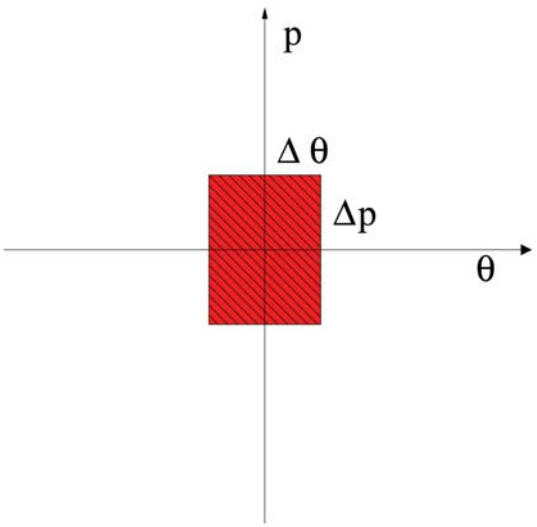

Fig. 30. Waterbag distribution.

the agreement was getting worse as the number of particles was increased, here $N = 20000$. This was contrasting with what was expected for a bona fide thermodynamic limit behavior. It took some time before the origin of this disagreement was understood. It was crucial to start with a simple set of initial conditions, that had a convenient parametrization. These are the "waterbags" in Fig. 30. The initial distribution of particles in the single-particle phase space (θ, p) is homogeneous within a rectangle of half sides $\Delta\theta$,Δp. Then, the initial energy and magnetization are directly related to $(\Delta\theta, \Delta p)$

$$m_0 = \frac{\sin\Delta\theta}{\Delta\theta}$$

$$\varepsilon = \frac{(\Delta p)^2}{6} + \frac{1 - (m_0)^2}{2} \, .$$

While energy is conserved, magnetization changes in time and reaches asymptotically its equilibrium value, predicted within the microcanonical ensemble. The time evolution of magnetization is shown in Fig. 31 for increasing values of N. The initial magnetization is zero because the initial state is homogeneous, $\Delta\theta = \pi$. One can observe an initial relaxation towards a state whose magnetization, as N increases, gets closer and closer to zero. This is what we will call a quasistationary state. At longer times, magnetization relaxes to the equilibrium value, which at this energy is $m \approx 0.3$. The lifetime of the quasistationary state increases with N, and

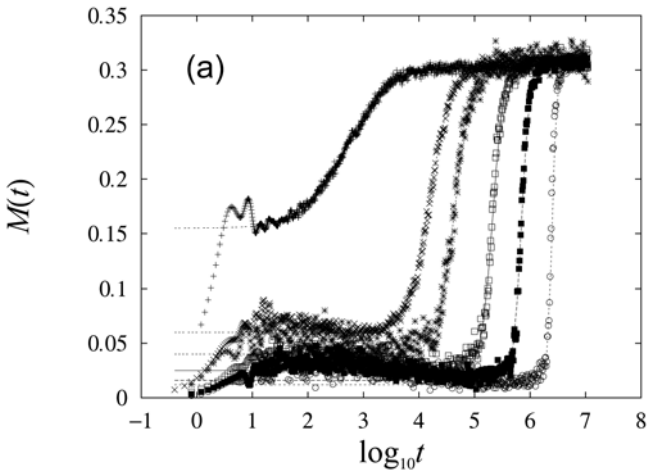

Fig. 31. Magnetization of the HMF model vs. time (in logarithmic scale) for $\Delta\theta = \pi$ and $\Delta p = 1.0677$, which gives an energy $\varepsilon = 0.69$. From left to right $N = 10^2, 10^3, 2 \times 10^3, 5 \times 10^3, 10^4, 2 \times 10^4$.

one can conjecture that it becomes infinite in the $N \to \infty$ limit. Therefore, in the thermodynamic limit, the system remains trapped in this quasistationary state and never reaches Boltzmann-Gibbs equilibrium. Indeed, we show in Fig. 32 that the lifetime of the quasistationary state depends on the number of particles as $N^{1.7}$.

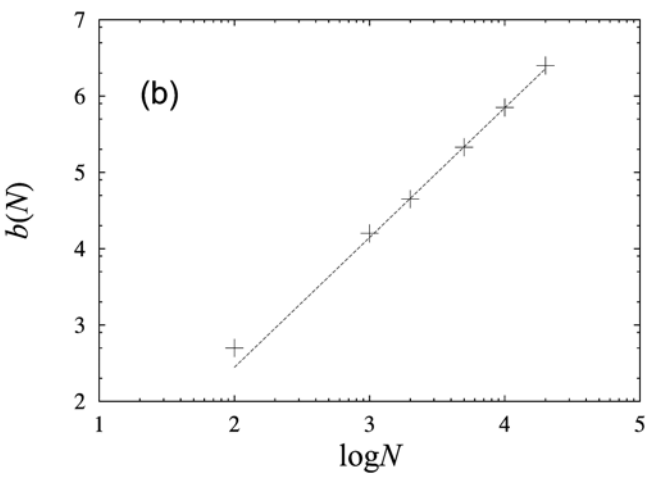

Fig. 32. Power-law dependence of the lifetime of the quasistationary state with respect to N. The best fit of the power is 1.7.

Where does this behavior come from? The origin is in the kinetic theory of model (117). Let us consider a slightly more general setting in which the potential is a generic periodic function V. The Hamiltonian is

$$H = \sum_{i=1}^{N} \frac{p_i^2}{2} + U(\theta_i) \quad , \quad U(\theta_1, \ldots, \theta_N) = \sum_{i<j}^{N} V(\theta_i - \theta_j) \,. \tag{118}$$

Let us introduce the discrete, one-particle, time dependent density function

$$f_d(\theta, p, t) = \sum_{i=1}^{N} \delta(\theta - \theta_i(t)) \delta(p - p_i(t)) \quad , \quad \int\int d\theta dp f_d = N \,. \tag{119}$$

Using the equations of motion and the property $x\delta(x-y) = y\delta(x-y)$, one gets the Klimontovich equation

$$\frac{\partial f_d}{\partial t} + p \frac{\partial f_d}{\partial \theta} - \frac{\partial v}{\partial \theta} \frac{\partial f_d}{\partial p} = 0 \,, \tag{120}$$

where

$$v(\theta, t) = \int d\theta' dp' V(\theta - \theta') f_d(\theta', p', t) \,. \tag{121}$$

The so-called empirical function (119) is highly singular. Let us then consider the smooth distribution $f(\theta, p, t)$ defined as

$$f_d = \langle f_d(\theta, p, t) \rangle + \delta f(\theta, p, t) = f(\theta, p, t) + \delta f(\theta, p, t) \,, \tag{122}$$

where the average $\langle \cdot \rangle$ is taken over initial conditions. The mean-field potential is then given by

$$v(\theta, t) = \langle v \rangle(\theta, t) + \delta v(\theta, t) \,, \tag{123}$$

where

$$\langle v \rangle(\theta, t) = \int d\theta' dp' V(\theta - \theta') f(\theta', p', t) \,. \tag{124}$$

After substituting eq. (122) into the Klimontovich equation (120) one gets the exact evolution equation

$$\frac{\partial f}{\partial t} + p \frac{\partial f}{\partial \theta} - \frac{\partial \langle v \rangle}{\partial \theta} \frac{\partial f}{\partial p} = \left\langle \frac{\partial \delta v}{\partial \theta} \frac{\partial \delta f}{\partial p} \right\rangle \,. \tag{125}$$

Simple scaling arguments allow us to prove that the r.h.s. of Eq. (125) is of order one, compared with the l.h.s., which is of order N. Then, in the $N \to \infty$ limit, Eq. (125) reduces to the Vlasov equation

$$\frac{\partial f}{\partial t} + p \frac{\partial f}{\partial \theta} - \frac{\partial \langle v \rangle}{\partial \theta} \frac{\partial f}{\partial p} = 0 \,. \tag{126}$$

Let us sketch this scaling argument. Let us impose that potential energy scales like kinetic energy (virial condition)

$$Np^2 \sim N^2 V_0 \tag{127}$$

where V_0 is the typical value of the potential energy per pair. Hence, $E \sim N^2 V_0$, $T \sim p^2 \sim N V_0$, $t_d \sim R/p \sim R/\sqrt{N V_0}$, where R is the typical size of the system and t_d a dynamical time. Let us now consider the thermodynamic limit in which $\varepsilon = E/(N^2 V_0)$, $T' = T/(N V_0)$ and $\tau_d = t_d \sqrt{N V_0}/R$ stay constant as $N \to \infty$. All this works fine if $N \to \infty$, $R \sim 1$, $E \sim N$, $T \sim 1$, $t_d \sim 1$ and $V_0 \sim 1/N$, this latter being the well known Kac trick. As for the reduced one-particle distribution function: $f/N \sim f_d/N \sim 1$, $v \sim 1$, $\delta f \sim 1/\sqrt{N}$, $\delta v \sim 1/\sqrt{N}$, which implies

$$\frac{1}{N} \left\langle \frac{\partial \delta v}{\partial \theta} \frac{\partial \delta f}{\partial p} \right\rangle \sim \frac{1}{N} \tag{128}$$

while f/N remains of order one.

On the other hand, the perturbation δf obeys the following equation

$$\frac{\partial \delta f}{\partial t} + p \frac{\partial \delta f}{\partial \theta} - \frac{\partial \delta v}{\partial \theta} \frac{\partial f}{\partial p} - \frac{\partial \langle v \rangle}{\partial \theta} \frac{\partial \delta f}{\partial p} = \frac{\partial \delta v}{\partial \theta} \frac{\partial \delta f}{\partial p} - \left\langle \frac{\partial \delta v}{\partial \theta} \frac{\partial \delta f}{\partial p} \right\rangle . \tag{129}$$

The l.h.s. of this equation is $O(\sqrt{N})$ while the r.h.s. is $O(1)$, hence we can neglect the r.h.s. in the large N limit (quasilinear theory). This corresponds to neglect higher order correlations (higher than those created by two-body collisions). If, moreover, we consider homogeneous states: $\partial f/\partial \theta = 0$, $\partial \langle v \rangle/\partial \theta = 0$, we obtain the coupled equations

$$\frac{\partial f}{\partial t} = \left\langle \frac{\partial \delta v}{\partial \theta} \frac{\partial \delta f}{\partial p} \right\rangle \quad , \quad \frac{\partial \delta f}{\partial t} + p \frac{\partial \delta f}{\partial \theta} - \frac{\partial \delta v}{\partial \theta} \frac{\partial f}{\partial p} = 0 . \tag{130}$$

In the adiabatic Bogoliubov approximation, the time evolution of δf (and, of course, of δv) is considered to be much faster than the time evolution of f itself. Therefore, one can neglect the time evolution of f when solving the equation for δf. Once δf and δv are obtained, they are inserted in the first equation, which then becomes a kinetic evolution equation for f, the so-called Lenard-Balescu equation. However, one can prove that in one dimension, as for our model (each particle has one degree of freedom), this procedure leads to the absence of evolution of f, i.e. the r.h.s. of the first of equations in (130) vanishes. One concludes that in one dimension, for homogeneous states, the time evolution of f is due to three-body and higher correlations.

All these considerations lead us to conclude that what we observe in Fig. 31 is a relaxation towards a Vlasov stable stationary state, called *violent* relaxation by the british astronomer D. Lynden-Bell, followed by a relaxation towards Boltzmann-

Gibbs, which is due to finite N "collisional" effects. The situation is well represented by the following diagram

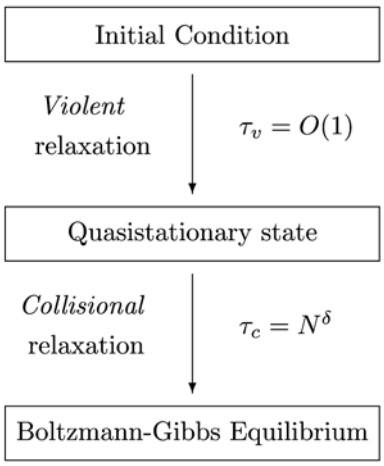

where $\delta = 1.7$ for our specific case.

Coming back to the HMF model, Vlasov equation reads

$$\frac{\partial f}{\partial t} + p\frac{\partial f}{\partial \theta} - \frac{dV}{d\theta}\frac{\partial f}{\partial p} = 0\,, \tag{131}$$

where

$$V(\theta)[f] = 1 - m_x[f]\cos(\theta) - m_y[f]\sin(\theta)\,,$$

$$m_x[f] = \int f(\theta, p, t)\cos\theta \,\mathrm{d}\theta\,\mathrm{d}p\,,$$

$$m_y[f] = \int f(\theta, p, t)\sin\theta \,\mathrm{d}\theta\,\mathrm{d}p\,.$$

It can be proven that the time evolution of a waterbag distribution, Fig. 30, under the Vlasov equation (131) is such that the area where the distribution is nonzero remains constant. The shape of the waterbag however changes, it is stretched and folded as shown in Fig. 33. This figure was drawn pictorially by Lynden-Bell, but it corresponds quite well to what happens in a numerical simulation, see Fig. 34. The lower right panel in Fig. 34 corresponds to the quasistationary state of the HMF model. Indeed, one obtains the same state by integrating the equations of motion deriving from Hamiltonian (117) on the same timescale. Let us consider a distribution that occupies uniformly a given area and divide the area into equal cells. In a dynamics which is compatible with area conservation, one can move an "occupied"

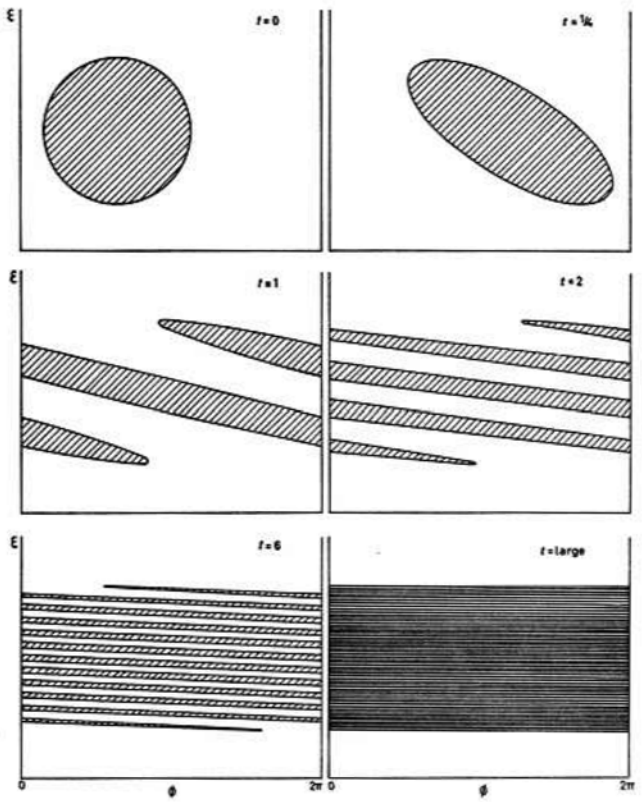

Fig. 33. Stretching and folding of a waterbag as pictorially represented by Lynden-Bell.

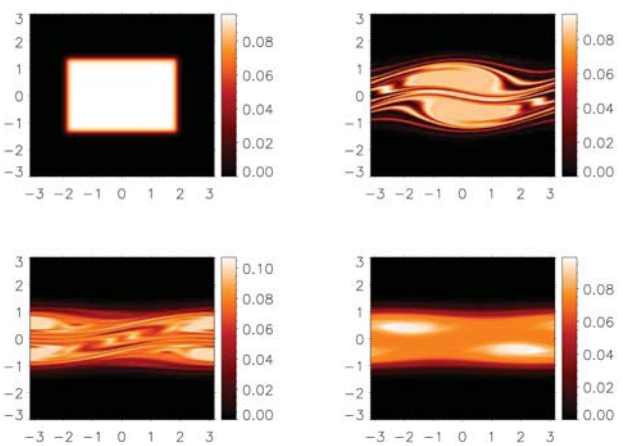

Fig. 34. Time evolution of a waterbag with $m_0 = 0.5$ and $\varepsilon = 0.69$. Time evolves from the upper left to the lower right panel.

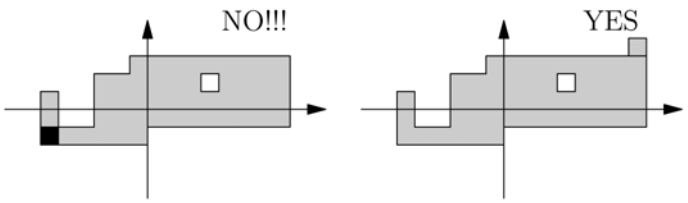

Fig. 35. Left panel: forbidden move of an occupied cell; Right panel: allowed move of an occupied cell.

cell into an "empty" cell, as shown in the upper panel of Fig. 35. On the contrary, one cannot move an occupied cell onto another occupied cell, because the total area would be reduced. This means that cells behave like fermions: a cell state can be either empty or occupied. This remark is at the basis of the construction of the Lynden-Bell entropy functional. One considers a set of macrocell made of smaller microcells, Fig. 36. Let us divide each macrocell into ν microcells of volume ω and consider a microscopic configuration in which the i-th macrocell is occupied by n_i microcells with level f_0 and $\nu - n_i$ with level zero. The total number of occupied microcells is $\mathcal{N}$, such that the total "mass" is $\mathcal{M} = \mathcal{N}\omega f_0$. This latter is also equal to

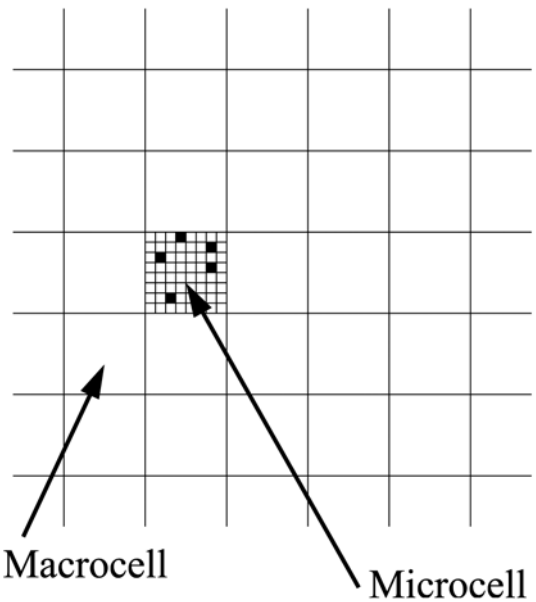

Fig. 36. Occupied microcells in a given macrocell for the construction of Lynden-Bell's entropy.

the normalization of the fine grained distribution $\mathcal{M} = \int d\theta dp f(\theta, p)$ (a convenient choice is $\mathcal{M} = 1$). The $\mathcal{N}$ occupied microcells are first placed into macrocells. There are $\mathcal{N}!/\prod_i n_i!$ ways to do this. Within the i-th macrocell, one can distribute the first of the n_i occupied microcells in ν ways, the second in $\nu - 1$ and so on. The number of ways of assigning the n_i occupied microcells is thus $\nu!/(\nu - n_i)!$. Then, the total number of microstates compatible with the macrostate where n_i microcells are occupied in macrocell i is given by the product of these two factors

$$W(\{n_i\}) = \frac{\mathcal{N}!}{\prod_i n_i!} \times \prod_i \frac{\nu!}{(\nu - n_i)!} \,. \tag{132}$$

The first factor is calculated exactly as for Boltzmann gas, because the occupied microcells are distinguishable, while the second factor reminds Fermi-Dirac statistics and derives from an exclusion principle, which is a consequence of fluid incompressibility: one microcell cannot be occupied more than once by an element of level f_0. Apart from this latter constraint, microcells are let to distribute freely among the different macrocells: this corresponds to making an assumption of ergodicity. This doesn't happen for the true Vlasov dynamics and is sometimes referred to as the hypothesis of efficient mixing. Using Stirling's approximation and expressing n_i in terms of the average probability to find level f_0 in cell i, $\rho_i(f_0) = n_i/\nu$, one obtains, neglecting an additive constant,

$$\ln W = \nu \sum_i \rho_i \ln \rho_i + (1 - \rho_i) \ln (1 - \rho_i) \,, \tag{133}$$

which can also be rewritten in terms of the coarse grained distribution function, $\rho_i = \bar{f}_i/f_0$. Taking the continuum limit $\sum_i \to \int d\theta dp/(\omega\nu)$, one finally gets the expression of Lynden-Bell's entropy for a two level distribution.

$$s_{LB}[\bar{f}] = -\int \frac{1}{\omega}\, d\theta dp \left[\frac{\bar{f}}{f_0} \ln \frac{\bar{f}}{f_0} + \left(1 - \frac{\bar{f}}{f_0}\right) \ln \left(1 - \frac{\bar{f}}{f_0}\right) \right] . \tag{134}$$

Maximizing Lynden-Bell's entropy at constant energy $\varepsilon[\bar{f}] = \int (p^2/2) \bar{f} d\theta dp + 1/2 - (m_x[\bar{f}]^2 + m_y[\bar{f}]^2)/2$ and momentum $P[\bar{f}] = \int p \bar{f} d\theta dp$ and taking into account "mass" $\mathcal{M}$ conservation, one gets the fermionic distribution

$$\bar{f}_{QSS}(\theta, p) = \frac{f_0}{e^{\beta(p^2/2 - m_y[\bar{f}_{QSS}] \sin\theta - m_x[\bar{f}_Q SS] \cos\theta) + \lambda p + \mu} + 1} \tag{135}$$

where $f_0 = 1/(4\Delta\theta\Delta p)$ and β, λ, μ are Lagrange multipliers associated with energy, momentum and "mass" conservation. The magnetization $(m_x[\bar{f}_{QSS}], m_y[\bar{f}_{QSS}])$ in the quasistationary state and the values of the multipliers are obtained by solving the self-consistent equations which follow by imposing the conservation laws mentioned

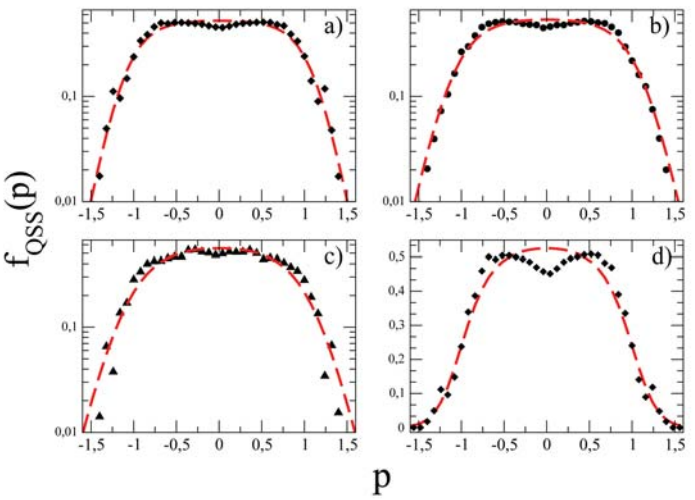

Fig. 37. Momentum distributions in the quasistationary state for $\varepsilon = 0.69$ and $m_0 = 0.3$ (panel a), $m_0 = 0.5$ (panel b),$m_0 = 0.7$ (panel c). The analytical results are plotted with a dashed red line, while the points are the results of numerical simulations. In panel d) the same distribution as in panel a) is plotted in a linear scale to make more visible the disagreement near the top: the double hump structure observed in the numerics is not reproduced by Lynden-Bell's theoretical approach.

above. The magnetization in the quasistationary state and the Lagrange multipliers are fully determined by the initial distribution.

In Fig. 37 we plot the momentum distribution in the quasistationary state obtained analytically (red dashed line) compared with those computed numerically. For all distributions in this figure, the magnetization in the quasistationary state is zero. The agreement is quite good, considering that the theoretical prediction is blind, no fitting parameter is used. However, as shown in panel d), this theoretical approach is unable to reproduce the double hump profile observed in numerics. This is a weakness of Lynden-Bell approach: the quality of the approximation cannot be determined a-priori. Another prediction of the theory is the existence of a phase transition in the (m_0, ε) plane. By varying these parameters of the initial distribution one either converges to a homogeneous, $m = 0$, or to an inhomogeneous, $m \neq 0$, quasistationary state. This situation is represented in Fig. 38 where the phase transition line (full black line), predicted theoretically, divides regions with non zero magnetization in the quasistationary state from regions with zero magnetization. The prediction is checked numerically by running the Vlasov equation for a mesh of values of (m_0, ε) and registering magnetization in the quasistationary state. Again, the prediction represents quite well the transition from homogeneous to inhomogeneous states. Analytically, one can show that the homogeneous state $(m_0 = 0)$ destabilizes at

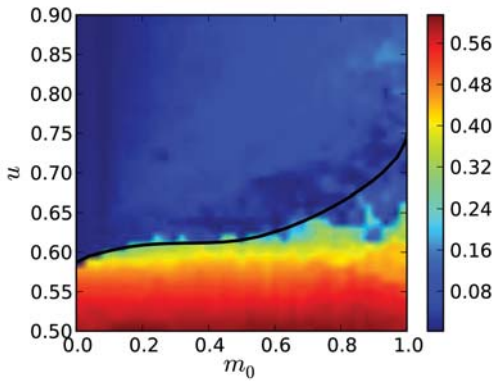

Fig. 38. Phase transition in the plane (m_0, ε).

$\varepsilon = 7/12$, in good agreement with numerics. The theory predicts a transition whose order changes at a tricritical point, while numerics and other theoretical approaches by Yan Levin and coworkers, seem to favor a first order transition everywhere.

Quasistationary states have been observed in a variety of systems, ranging from self-gravitating systems to plasmas. We here give a further illustration, showing their presence in the model of free electron laser introduced above, (43). In Fig. 39 we plot the laser intensity A vs. time. Initially, this quantity grows exponentially, but then it convergence (with damped oscillations) to the quasistationary state. However, for the

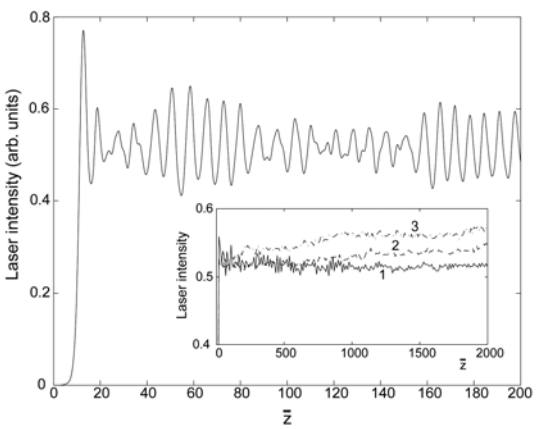

Fig. 39. Laser intensity vs. time for the free electron laser model (43). In the main plot, we show the short time exponential growth and the successive convergence to the quasistationary state for $N = 5000$. In the inset, we plot the intensity for three different values of N at later times: $N = 5000$ (full line), $N = 400$ (dashed line), $N = 100$ (dash-dotted line).

smaller values of N shown in the inset, the convergence to the quasistationary state is followed by a successive "collisional" evolution towards Boltzmann-Gibbs equilibrium.

The Vlasov equation for the free electron laser model reads

$$\frac{\partial f}{\partial z} = -\, p\,\frac{\partial f}{\partial \theta} + 2(A_x \cos\theta - A_y \sin\theta)\,\frac{\partial f}{\partial p}\,,$$

$$\frac{\partial A_x}{\partial z} = -\,\delta A_y + \frac{1}{2\pi}\int f \cos\theta\, d\theta dp\,,$$

$$\frac{\partial A_y}{\partial \bar{z}} = \delta A_x - \frac{1}{2\pi}\int f \sin\theta\, d\theta dp\,,$$

with $\mathbf{A} = A_x + iA_y = \sqrt{I}\exp(-i\varphi)$.

Lynden-Bell entropy (134) maximization

$$s_{LB}(\varepsilon,\sigma) = \max_{\bar{f},A_x,A_y} [s_{LB}(\bar{f}) | H(\bar{f},A_x,A_y) = N\varepsilon; \int d\theta dp \bar{f} = 1; P(\bar{f},A_x,A_y) = \sigma] \tag{136}$$

gives the stationary coarse-grained distribution

$$\bar{f} = f_0 \frac{e^{-\beta(p^2/2 + 2A\sin\theta) - \lambda p - \mu}}{1 + e^{-\beta(p^2/2 + 2A\sin\theta) - \lambda p - \mu}} \tag{137}$$

with quasistationary laser intensity

$$A = \frac{\beta}{\beta\delta - \lambda}\int dp d\theta \sin\theta \bar{f}(\theta,p)\,. \tag{138}$$

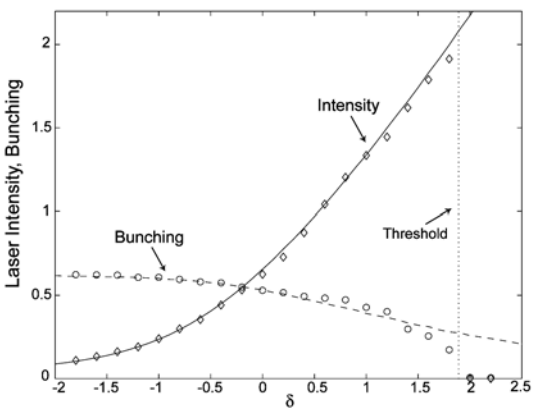

Fig. 40. Laser intensity A and bunching parameter $\sum_i \cos\theta_i/N$ vs. detuning δ in the quasistationary state for a model of free electron laser. The lines are the predictions of Lynden-Bell theory and the points the results of numerical simulations.

Again, λ, μ, β and f_0 are obtained by solving a set of implicit equations similar to those obtained for the HMF model. The comparison of the quasistationary values of laser intensity and electron bunching parameter with numerical results is shown in Fig. 40. This theoretical result is ready for an experimental test either in free electron lasers or in cold atoms in a cavity.

Acknowledgments. The authors acknowledge support by INFN and by ANR-10-CEXC-010-01, Chaire d'Excellence project. The authors also thank the organizers of the summer school where this work was presented, in particular Roberto Monaco, for the kind invitation. The environment of the school was particularly pleasant, not only the natural environment but also the scientific one. The students were always asking very interesting questions that helped the lecturer (SR) improve his knowledge in the field.

References

[1] A. CAMPA, T. DAUXOIS and S. RUFFO, *Statistical mechanics and dynamics of solvable models with long-range interactions*, Phys. Rep. **480** (2009), 57-159.

[2] T. DAUXOIS, S. RUFFO, E. ARIMONDO and M. WILKENS Eds., *Dynamics and thermodynamics of systems with long-range interactions: an introduction*, Lecture Notes in Phys., **602**, Springer, Berlin 2002.

[3] T. DAUXOIS, S. RUFFO and L. F. CUGLIANDOLO, eds., *Long-range interacting systems,* Oxford University Press, Oxford 2010.

AURELIO PATELLI
University of Florence
Department of Physics and Astronomy
via G. Sansone, 1
Sesto Fiorentino, 50019, Italy
e-mail: oreca85@gmail.com

STEFANO RUFFO
University of Florence
Department of Physics and Astronomy
via G. Sansone, 1
Sesto Fiorentino, 50019, Italy
e-mail: stefano.ruffo@unifi.it